Chapter 4

The Formation of Population III stars in a ΛCDM universe

4.1 Summary

In this chapter I discuss aspects of primordial star formation in a ΛCDM universe. The collapse of gas in a representative halo which will contain a single Population III protostar is described in detail in Section 4.4.1, emphasizing the critical role that the chemistry and cooling properties of molecular hydrogen gas (H_2) play. Our results are both qualitatively and quantitatively similar to those discussed in Abel, Bryan & Norman [39] despite being in a different cosmology. Section 4.4.2 describes the role of angular momentum in the formation of primordial protostars for the same halo, showing that the gas which collects in the halo core preferentially has low angular momentum compared to gas that does not collapse into the center of the halo. I analyze angular momentum transport in the halo using standard disk methods as well as by using Lagrangian "tracer particles" and show that some angular momentum transport also appears to take place during the collapse of the halo through turbulent transport. The disk approximation is a poor one, however, since the molecular cloud-like objects that form in the center of the halos are spheroidal in shape and generally have circular velocities that are far lower than the Keplerian circular velocity.

In Section 4.4.3, I examine the consistency of radial properties of halos which form Population III stars when the simulation volume and the large scale structure are varied. A dozen simulations are examined using three different box sizes. The simulations are compared when the gas at the center of the halo has reached $\sim 10^{11}$ cm^{-3}. Simulations with the same box size but different large scale structure show comparable evolution of the first protostar to form in each calculation,, though with significant scatter in properties such as the core temperature and accretion rate onto the central protostar. Simulations with different box sizes show a systematic trend towards higher molecular

hydrogen fractions, lower baryon temperatures, and lower overall accretion rates onto the primordial protostar with increasing box size. This result is robust and suggests that previous estimates of the Population III mass range from three-dimensional cosmological calculations may overestimate the Population III mass function by a significant amount.

Section 4.4.4 explores the formation of Population III stars in the presence of a soft UV (SUV) background. I use a single cosmological realization and vary the SUV background over a wide range of values. I show that for a significant range of the SUV background fluxes the main effect of this background is to delay the collapse of the primordial cloud by inhibiting the formation of molecular hydrogen. The final properties of the Population III protostar are quite similar regardless of the UV background strength, though final accretion rates vary nonlinearly with the SUV background flux. Halos subject to very high soft UV background fluxes do not form enough H_2 to collapse during the simulation, which implies that a different mode of primordial star formation must take place when the UV background is very high.

4.2   Motivation

As discussed in Section 1.3, many unresolved issues remain concerning the formation of Population III stars. Exploration of the detailed properties of these objects via purely analytical work is essentially impossible due to the wide range of physics involved, which includes the dynamics of dark matter systems, hydrodynamics, and the nonequilibrium chemistry and radiative cooling of the primordial gas out of which these objects form. Similarly, simulations have shown that the formation process of Population III stars is not inherently symmetrical, and that the formation of these stars takes place in a cosmological context. This suggests that in order to correctly model the formation of Population III stars, we need three-dimensional simulations with extremely high spatial and temporal dynamical range.

Previously published three dimensional, high dynamical range cosmological simulations of the formation of Population III stars (Abel, Bryan and Norman [39], hereafter ABN) are an important step towards understanding these objects. This work was performed in a $\Omega_m = 1$ universe, and derives results about the possible mass function of Population III stars using only one cosmological realization in a relatively small (128 h^{-1} kpc) simulation volume. In this chapter I explore the formation of Population III protostars in a ΛCDM universe, using multiple box sizes and cosmological realizations, in order to determine the robustness of the predictions in ABN.

Another important scenario for the formation of Population III stars involves the presence of a soft ultraviolet (SUV) background. Massive primordial stars are copious emitters of ultraviolet radiation, particularly in the Lyman-Werner energy band ($11.18 - 13.6$ eV) which is responsible for the photodissociation of molecular hydrogen. Since

this radiation is below the ionization energy of atomic hydrogen it is probable that photons in the Lyman-Werner band form a background of soft ultraviolet light, which could significantly affect the formation of later generations of Population III stars via the dissociation of molecular hydrogen. Previous work has been done on this subject by Machacek, Bryan & Abel [71] – however, the work presented here uses higher resolution calculations and examines more fully the evolution of a single halo.

4.3   Problem setup

All of the simulations described in this chapter are performed using the adaptive mesh cosmology code Enzo, which is described in detail in Section 2.2. They are initialized at $z = 99$ assuming a "concordance" cosmological model: $\Omega_m = 0.3$, $\Omega_b = 0.04$, $\Omega_{CDM} = 0.26$, $\Omega_\Lambda = 0.7$, $h = 0.7$ (in units of 100 km/s/Mpc), $\sigma_8 = 0.9$, and using an Eisenstein & Hu power spectrum [194] with a spectral index of $n = 1$. The selection of CDM power spectrum is unimportant, as at the length scales being explored in these calculations the power spectrum effectively becomes a power law with $P(k) \sim k^{-3}$ for all plausible CDM power spectra. Twelve simulations are generated using a separate random seed for each, meaning that the large-scale structure that forms in each of the simulation volumes is statistically independent of the others. These simulations are divided into sets of four simulations in three different box sizes: $0.3, 0.45$, and 0.6 h^{-1} Mpc (comoving). The first halo to form in each simulation with a mass of $\sim 10^6$ M$_\odot$ is found using a dark matter-only calculation with 128^3 particles on a 128^3 root grid with a maximum of 4 levels of adaptive mesh, refining on a dark matter overdensity criterion of 8.0. The initial conditions are then regenerated with both dark matter and baryons for each of the simulation volumes such that the Lagrangian volume in which the halo formed is now resolved at much higher spatial and mass resolution using the nested initial condition method described in Section 2.1.2. These simulations have a 128^3 root grid and three static nested grids, for an overall effective grid size of 1024^3 in the region where the most massive halo will form. The highest resolution grid in each simulation is 256^3 grid cells, and corresponds to a volume $(75, 112.5, 150)$ h^{-1} comoving kpc on a side for the $(0.3, 0.45, 0.6)$ h^{-1} Mpc box. The dark matter particles in the highest resolution grid are $(1.81, 6.13, 14.5)$ h^{-1} M$_\odot$ and the spatial resolution of cells on these grids are $(293, 439, 586)$ h^{-1} parsecs (comoving). Though the simulations have a range of initial spatial resolutions and dark matter masses, we find that the final simulation results are converged – the spatial and mass resolution of the 0.3 h^{-1} Mpc volume simulations can be degraded to that of the 0.6 h^{-1} Mpc without significantly changing the results.

The simulations are then started at $z = 99$ and allowed to evolve until the collapse of the gas within the center of the most massive halo, which occurs at a range of redshifts (as shown in Section 4.4.3). The equations of hydrodynamics are solved using the PPM

method with a dual energy formulation, as described in Section 2.2.2 (the results are the same when the ZEUS hydrodynamic method is used). The nonequilibrium chemical evolution and optically thin radiative cooling of the primordial gas is modeled as described in Section 2.2.5, following 9 separate species including molecular hydrogen (but excluding deuterium). Adaptive mesh refinement is turned on such that cells are refined by factors of two along each axis, with a maximum of 22 total levels of refinement. This corresponds to a maximum resolution of (115, 173, 230) h^{-1} astronomical units (comoving) at the finest level of resolution, with an overall spatial dynamical range of 5.37×10^8. To avoid effects due to the finite size of the dark matter particles, the dark matter density is smoothed on a comoving scale of ~ 0.5 pc. This is reasonable because at that radius in all of our calculations the gravitational potential is dominated by the baryons.

Grid cells are adaptively refined based upon several criteria: baryon and dark matter overdensities in cells of 4.0 and 8.0, respectively, checks to ensure that the pressure jump and/or energy ratios between adjoining cells never exceeds 5.0, that the cooling time in a given cell is always longer than the sound crossing time of that cell, and that the Jeans length is always resolved by at least 16 cells. This guarantees that the Truelove criterion [217], which is an empirical result showing that in order to avoid artificial fragmentation in numerical simulations the Jeans length must be resolved by at least 4 grid cells, is always maintained by a comfortable margin. Simulations which force the Jeans length to be resolved by a minimum of 4 and 64 cells produce results which are essentially identical to when the Jeans length is resolved by a minimum of 16 cells.

The simulations described in Section 4.4.4 take one of the models described previously (with a box size of 0.3 h^{-1} Mpc) and resimulate it assuming a range of unevolving soft UV backgrounds with intensities in the Lyman-Werner band of $F_{LW} = 0.0, 10^{-24}, 10^{-23}, 3 \times 10^{-23}, 10^{-22}, 10^{-21}$ and 10^{-20} erg s^{-1} cm^{-2} Hz^{-1}. This covers a much wider range of parameter space than the results described in Machacek, Bryan & Abel [71]. As with the other calculations, these are initialized at $z = 99$ and evolved until the collapse of the core of the largest halo, which occurs at a range of redshifts. The simulations with the two highest SUV fluxes do not collapse before $z = 10$, the point at which the simulations are stopped.

4.4 Results

4.4.1 Collapse of a representative primordial star

In this section we describe in detail the collapse of a single primordial protostar out of the ensemble discussed in Section 4.4.3. This simulation was selected at random out of the four simulations performed in a 0.3 h^{-1} Mpc comoving volume. The results described here are qualitatively similar for all of the calculations described in Section 4.4.3, though there is some scatter in the exact evolution of each halo due to differences in large scale

structure and the detailed merger history of the halo. However, since the collapse is essentially controlled by the chemistry of molecular hydrogen formation, the result is general.

Figures 4.1, 4.2, and 4.3 zoom in on the central gas core in each halo at the redshift of collapse by factors of four, showing projections of log baryon density, log baryon temperature, and maximum refinement level, respectively. The largest-scale panel shows a projection of a volume of the universe 1320 proper parsecs across and deep, and zooms in to approximately 1.3 pc across. Each panel is centered on the collapsing protostar. At large scales it is apparent from Figure 4.1 that the halo in which the first star in the simulation volume forms is at the intersection of two cosmological filaments, a distinctly asymmetrical situation. Examination of Figure 4.2 shows that the filaments and majority of the volume of the halo are relatively hot (~ 1000 Kelvin), due primarily to accretion shocks formed by gas raining onto the filaments and into the halo. However, as we zoom in towards the center of the halo we can see that the high-density gas is at a much lower temperature (a few hundred Kelvin) due to cooling by the significant quantity of molecular hydrogen that is formed in the halo. The gas within the halo is not particularly spherical until scales of a few parsecs are reached, where a slightly warmer core of gas forms with an overall mass of a few thousand solar masses, harboring a fully-molecular protostar with a mass of ~ 1 M$_\odot$. The central core is generally spheroidal due to gas pressure and is not rotationally supported at any point. Figure 4.3 shows how the adaptive mesh refinement is used to resolve the cosmological structure by concentrating refinement only where it is needed. This method is extremely effective at conserving computational resources - the level 16 grids, which are the highest level of resolution shown in Figure 4.3, only encompass $\sim 2.5 \times 10^{-17}$ of the overall volume!

Figures 4.4 through 4.7 show the evolution of radial profiles of several spherically averaged, mass-weighted baryon quantities of a representative primordial protostar from approximately the onset of halo collapse until the formation of a fully molecular protostar. The halo begins its collapse at $z = 18.05$ (approximately 2.04×10^8 years after the Big Bang) and ends its collapse 6.294×10^6 years later, at $z = 17.67$. Figure 4.4 shows the spherically-averaged baryon number density, temperature, and enclosed mass as a function of radius. Figure 4.5 shows the molecular hydrogen fraction, electron fraction, and H^- fraction as a function of radius. Figure 4.6 shows the evolution of angular momentum as a function of enclosed mass, baryon radial velocity as a function of radius, and circular velocity of the cloud as a function of radius. Figure 4.7 shows the ratios of gas cooling time to sound crossing time, cooling time to system dynamical time, and sound crossing time to dynamical time as a function of radius. The lines in all of these plots are color coded such that the same line color and type corresponds to the same time in each panel.

We begin to follow the evolution of the halo at $z = 18.05$, when the central hydrogen number density has reached $n \sim 10^3$ particles per cubic centimeter (black solid line in
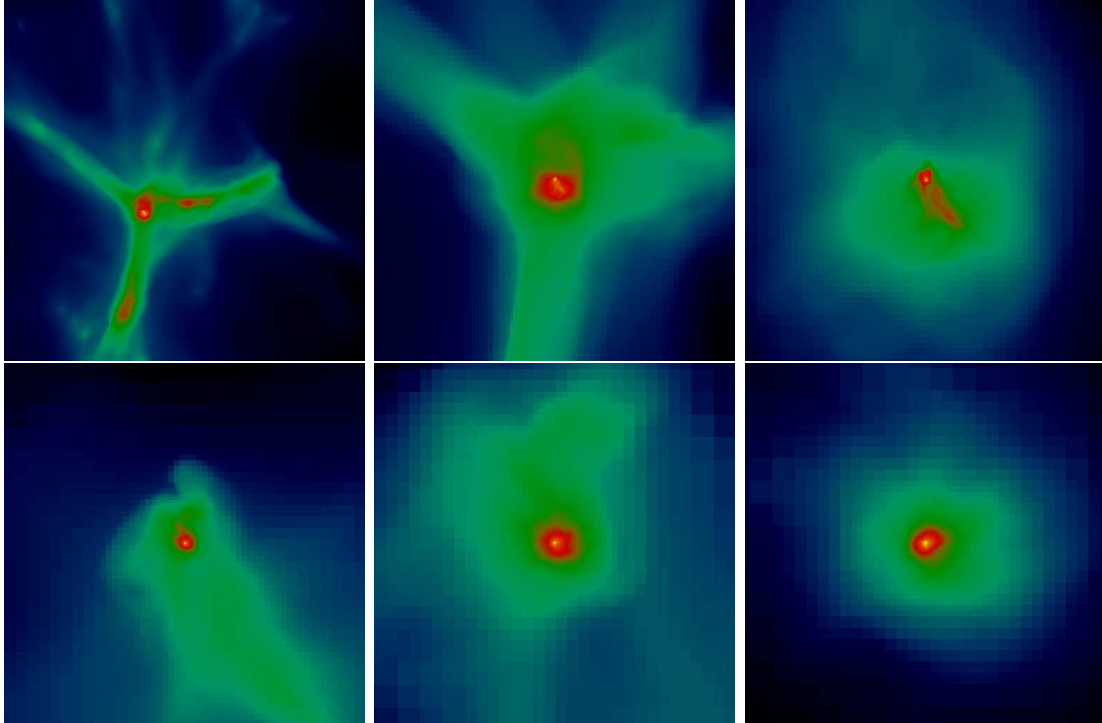
Figure 4.1: Zoom on projected mass-weighted baryon density by factors of four for a representative Population III protostar formation calculation at the last simulation output. At this redshift ($z = 19.28$), the maximum density was $\sim 10^{12}$ cm^{-3} with a cosmic mean density of $\simeq 0.003$ cm^{-3}, for an overall density increase of 15 orders of magnitude. Top left: view is 1320 pc across. Top center: 330 pc. Top right: 82.5 pc. Bottom left: 20.6 pc. Bottom center: 5.2 pc. Bottom right: 1.29 pc. Note that all sizes are in proper parsecs at $z = 19.28$. In all panels yellow represents high densities and blue represents low density, with the color table relative in each frame.
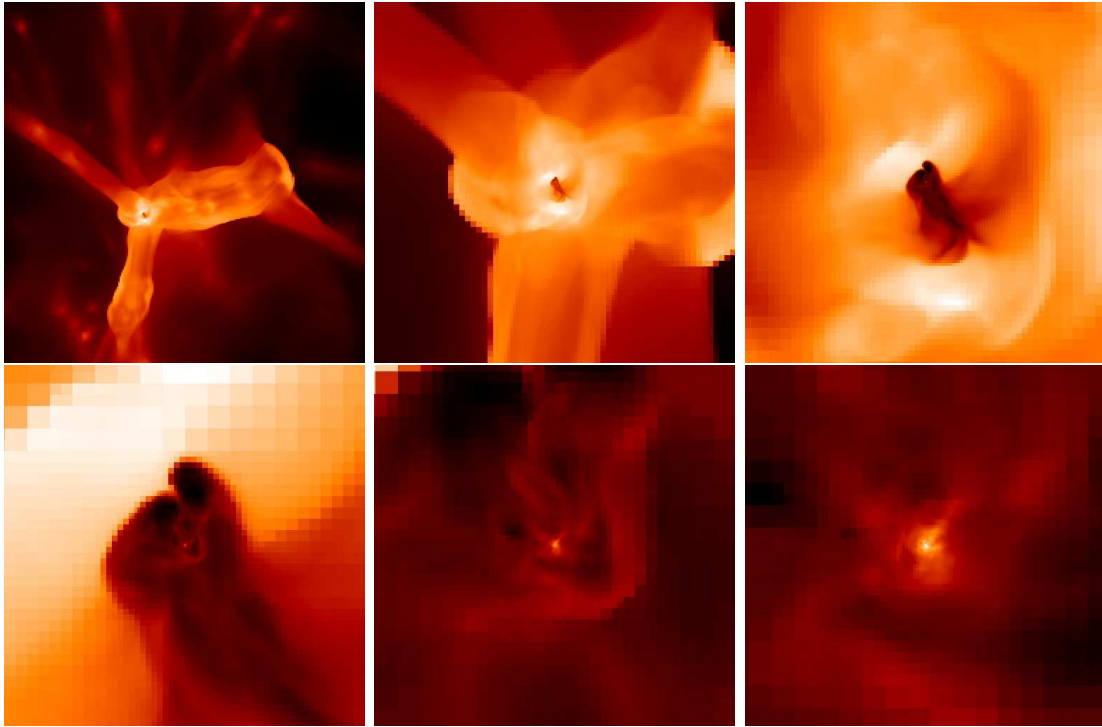
Figure 4.2: Zoom on projected mass-weighted baryon temperature by factors of four in a representative Population III protostar formation calculation at the last simulation output. The collapse redshift is $z = 19.28$ and the simulation and spatial sizes of each panel are the same as in Figure 4.1. In all panels white represents high temperatures and dark colors represent low temperatures. The color table is relative in each frame.
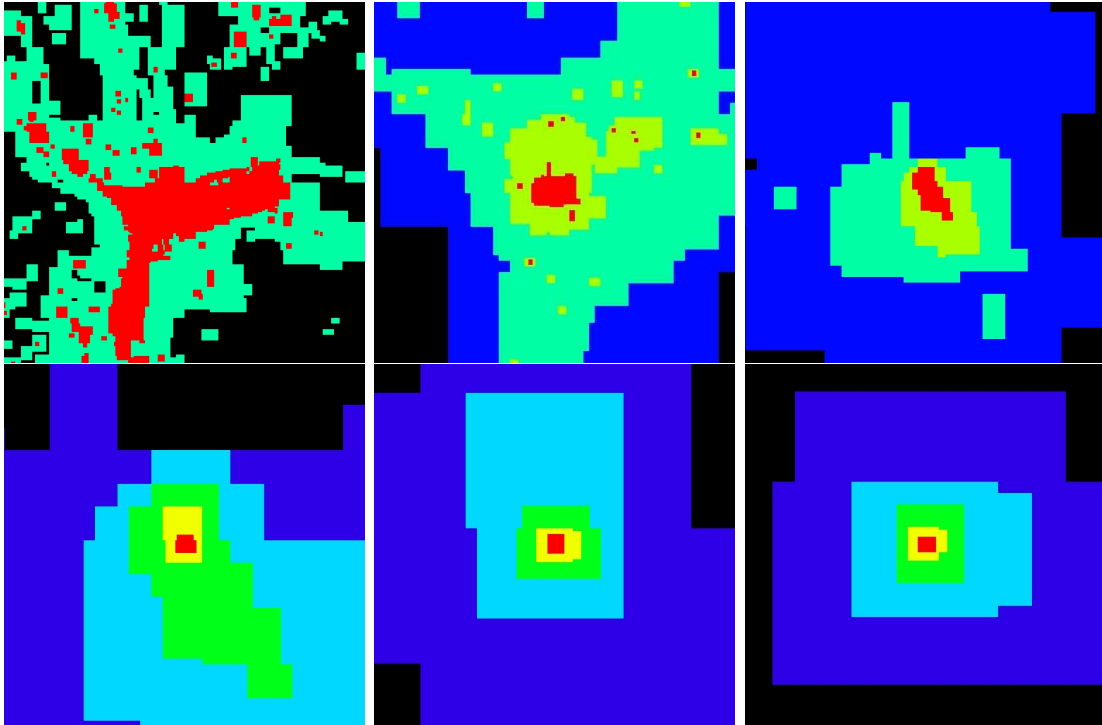
Figure 4.3: Zoom on projected maximum level in a representative Population III protostar formation calculation at the last simulation output. The spatial scale for each panel and simulation are the same as in Figure 4.1. The maximum projected level in each panel is as follows. Top left: Level 6. Top center: Level 8. Top right: Level 10. Bottom left: Level 12. Bottom center: Level 14. Bottom right: Level 16. In each panel the highest level grid is represented is in red, second highest in yellow, and so on. The highest level of resolution at this time is $L = 22$.

all plots). This corresponds to a core with a radius of ~ 1 parsec and a mass of a few thousand solar masses, which is accreting gas at a significant rate. The molecular hydrogen fraction within this core is slightly less than 10^{-3} but is still enough to rapidly cool the center of the halo to ~ 200 Kelvin at a cooling rate proportional to the square of the gas density. The gas cannot cool below this temperature because of the sharp decrease in the cooling rate of molecular hydrogen below $\simeq 200$ Kelvin. This core is the high-redshift equivalent of a molecular cloud core. The halo "loiters" for approximately six million years as the amount of molecular hydrogen is slowly built up to a mass fraction of a few times 10^{-3} and the central density increases. As the gas density passes roughly $n \sim 10^4$ cm^{-3} the ro-vibrational levels of H$_2$ are populated at their equilibrium value and the cooling rate again becomes independent of density, which corresponds to an increase in gas temperature with increasing density (as can be seen by the blue and green solid lines in the temperature vs. radius plot in Figure 4.4). As the temperature increases the cooling rate again begins to rise, leading to an increase in the inflow velocities of gas. Examination of the plot of enclosed mass vs. radius in Figure 4.4 shows that at this point the enclosed gas mass has exceeded the Bonnor-Ebert critical mass, which is defined as $M_{BE} = 1.18 M_\odot (c_s^4/G^{3/2}) P_{ext}^{-1/2}$, where c_s is the local sound speed and G is the gravitational constant. This is the critical mass at which an isothermal sphere of gas with an external pressure P_{ext} becomes unstable and undergoes collapse. This occurs in this halo at a mass scale of ~ 1000 M$_\odot$.

When the central density of the cloud core becomes sufficiently large ($n \sim 10^8$ cm^{-3}) the three-body H$_2$ formation process takes over, resulting in a rapid increase in the molecular hydrogen fraction from a few times 10^{-3} to essentially unity. This causes a huge increase in the cooling rate, which results in a rapid drop in temperature of the center of the halo, allowing it to contract and causing an increase in central density of $n \sim 10^{15}$ cm^{-3} in only another $\sim 2 \times 10^4$ years, with a corresponding increase in the inflow rates. At a mass scale of ~ 1 M$_\odot$ a protostellar core forms which is completely molecular and has gas accreting onto it supersonically, producing a protostellar accretion shock at ~ 100 astronomical units from its center. At this point the optical depth of the halo core becomes close to unity to molecular hydrogen ro-vibrational line emission, so we terminate the simulation because the assumption of optically thin radiative cooling used in our code is no longer correct.

It is useful to examine the relevant chemical, thermal and dynamical timescales of the collapsing halo. The ratios of cooling time to sound crossing time (calculated in spherically averaged radial shells) as a function of radius, cooling time to dynamical time, and sound crossing time to dynamical time are plotted in Figure 4.7. Within the core of the halo ($r \sim 1$ parsec) the sound crossing time (t_{cross}) is slightly less than the dynamical time (t_{dyn}) for the majority of the evolution time of the halo, while the cooling time (t_{cool}) is somewhat longer than both of these timescales (but generally only by a factor of a few). If $t_{cross} \ll t_{dyn}$ the halo is stable against collapse because the halo

can easily equilibrate its pressure to compensate for collapsing gas. If $t_{cross} \gg t_{dyn}$, the system cannot come into equilibrium and is in free-fall. In this case, $t_{cross} \approx t_{dyn} < t_{cool}$, and the system is undergoing a quasistatic collapse. This can also be seen by examining the evolution of the radial infall velocity as a function of radius in Figure 4.6, where the radial infall velocity is subsonic until the very last portion of the core's evolution, when it becomes locally supersonic. This corresponds to a dramatic increase in the molecular hydrogen fraction, and a corresponding rapid decrease in the cooling time. In the center of the halo at the last few data outputs, the cooling time becomes shorter than both the dynamical time and sound crossing time, creating a situation where gas is essentially free-falling onto the central protostar.

As in ABN, we carefully examine the forming protostellar core for signs of fragmentation. This might be expected due to chemothermal instabilities caused by the rapid formation of molecular hydrogen via the 3-body process and the resulting rapid increase in cooling rate. However, the sound crossing time within the core is less than the H_2 formation timescale until the last output time, allowing mixing to take place and preventing the formation of large density contrasts. By the time that the H_2 formation timescale becomes shorter than the sound crossing time, the core is fully molecular and therefore stable against this chemothermal instability.

As discussed previously, at the time that the simulation is stopped (due to a breakdown in the assumption of optically thin radiative cooling at the center of the protostellar cloud) a fully-molecular protostar with a mass of ~ 1 $M_\odot$ has formed and is accreting gas supersonically. The spherically-averaged accretion time at the last output timestep, plotted as a function of enclosed gas mass, is shown as the red solid line in Figure 4.8. The accretion time is defined as $t_{acc} \equiv M_{enc}/\dot{M}$, where M_{enc} is the enclosed baryon mass and $\dot{M} \equiv 4\pi r^2 \rho(r) v(r)$, with $\rho(r)$ and $v(r)$ being the baryon density and velocity as a function of radius, and $v(r)$ defined as being positive towards the center of the halo. The green solid line the accretion time as determined by taking the local accretion rate from the Shu isothermal collapse model, $\dot{M}_{Shu} = m_0 c_s^3/G$, where m_0 is a dimensionless constant of order unity, c_s is the sound speed, and G is the gravitational constant. This value of $\dot{M}$ is calculated in each bin and the accretion time is plotted as $M_{enc}/\dot{M}_{Shu}$. The dot-long dashed line is the Kelvin-Helmholz time for a Population III star with a mass identical to the enclosed mass, as calculated from the results given by Schaerer [59]. The dot-short dashed line is the baryon accretion time for the result in Abel, Bryan, and Norman.

The agreement between the spherically-averaged accretion rate and that estimated by the Shu isothermal collapse model is striking. As shown by Shu [204], as long as the densities in a condensing molecular cloud core span several orders of magnitude before a stage of dynamic instability is reached, the subsequent collapse properties of the cloud should resemble those of an isothermal sphere. The lack of characteristic time and length scales results in a self-similar wave of infalling gas which propagates outward
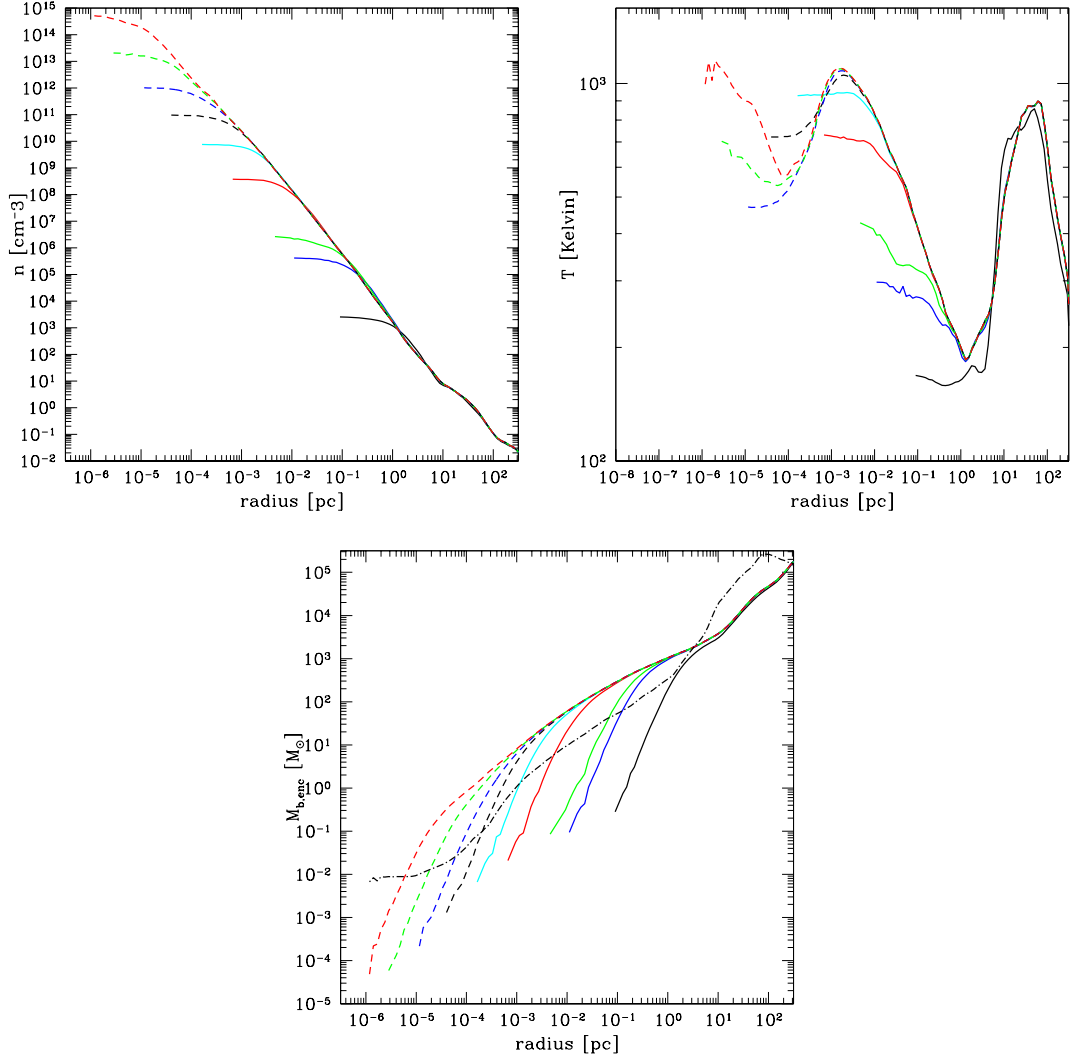
Figure 4.4: Evolution of spherically-averaged values for baryon number density (top left), baryon temperature (top right), and enclosed baryon mass (bottom) as a function of radius of a representative primordial protostar. The solid black line in each panel corresponds to spherically averaged radial profile of each quantity the onset of halo collapse, at $z = 18.05$ (approximately 2.04×10^8 years after the Big Bang). Solid blue line: the state of the halo 8.73×10^5 years after that. Solid green line: 5.103×10^6 years later. Solid red line: 2.99×10^5 years later. Solid cyan line: $16,660$ years later. Dashed black line: 2267 years later. Dashed blue line: 310 years later. Dashed green line: 91 years later. Dashed red line: 31 years later, at a final output redshift of $z = 17.673$. The total time spanned by the lines in these panels is 6.294×10^6 years. The black dot-dashed line in the bottom left panel is the Bonnor-Ebert critical mass calculated at the last timestep.
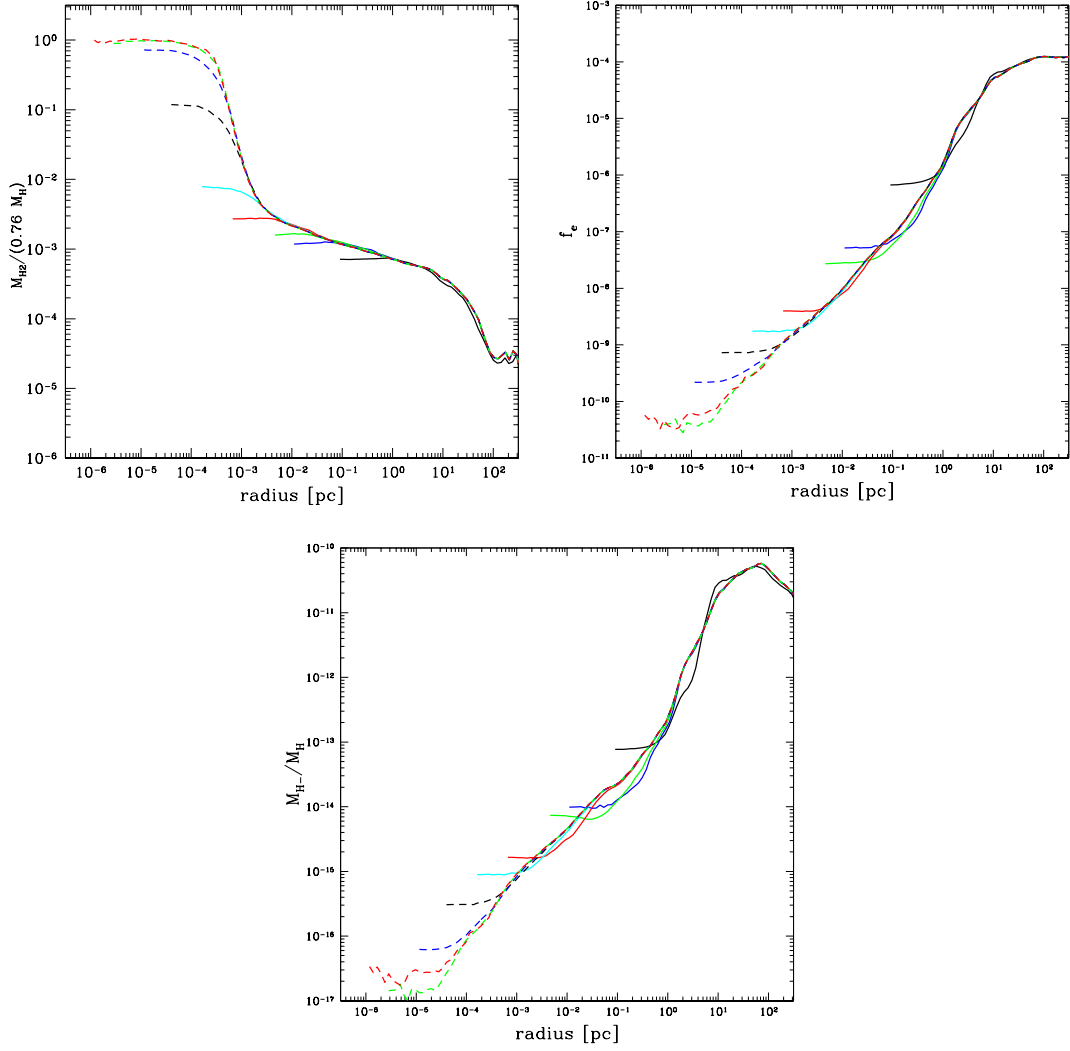
113

Figure 4.5: Evolution of spherically averaged radial profiles of molecular hydrogen fraction (top left), electron fraction (top right), and H^- fraction (bottom) as a function of radius of a representative primordial protostar. The lines correspond to the same times as in Figure 4.4 and are of the same simulation.
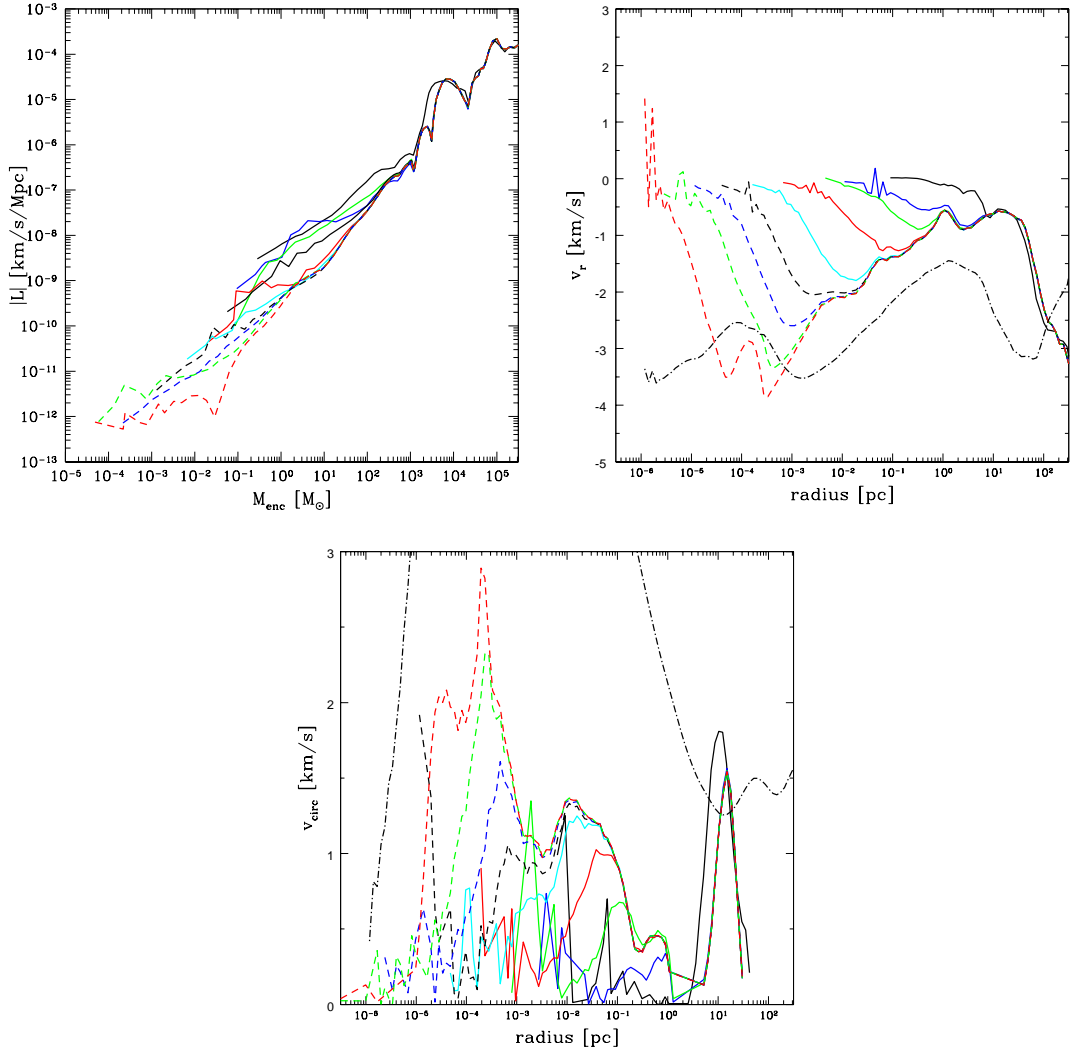
Figure 4.6: Evolution of radial profiles of spherically-averaged baryon angular momentum as a function of enclosed mass of a representative primordial protostar (top left panel) and radial velocity and circular velocity as a function of radius (top right and bottom panels, respectively). The lines correspond to the same times as in Figure 4.4 and are of the same simulation. The black dot-dashed line in the plot of radial velocity as a function of radius is the sound speed calculated using the local baryon temperature in each radial bin at the last simulation timestep. The black dot-dashed line in the plot of baryon circular velocity vs. time is the Newtonian circular velocity computed from the radius and enclosed baryon mass at the last timestep.
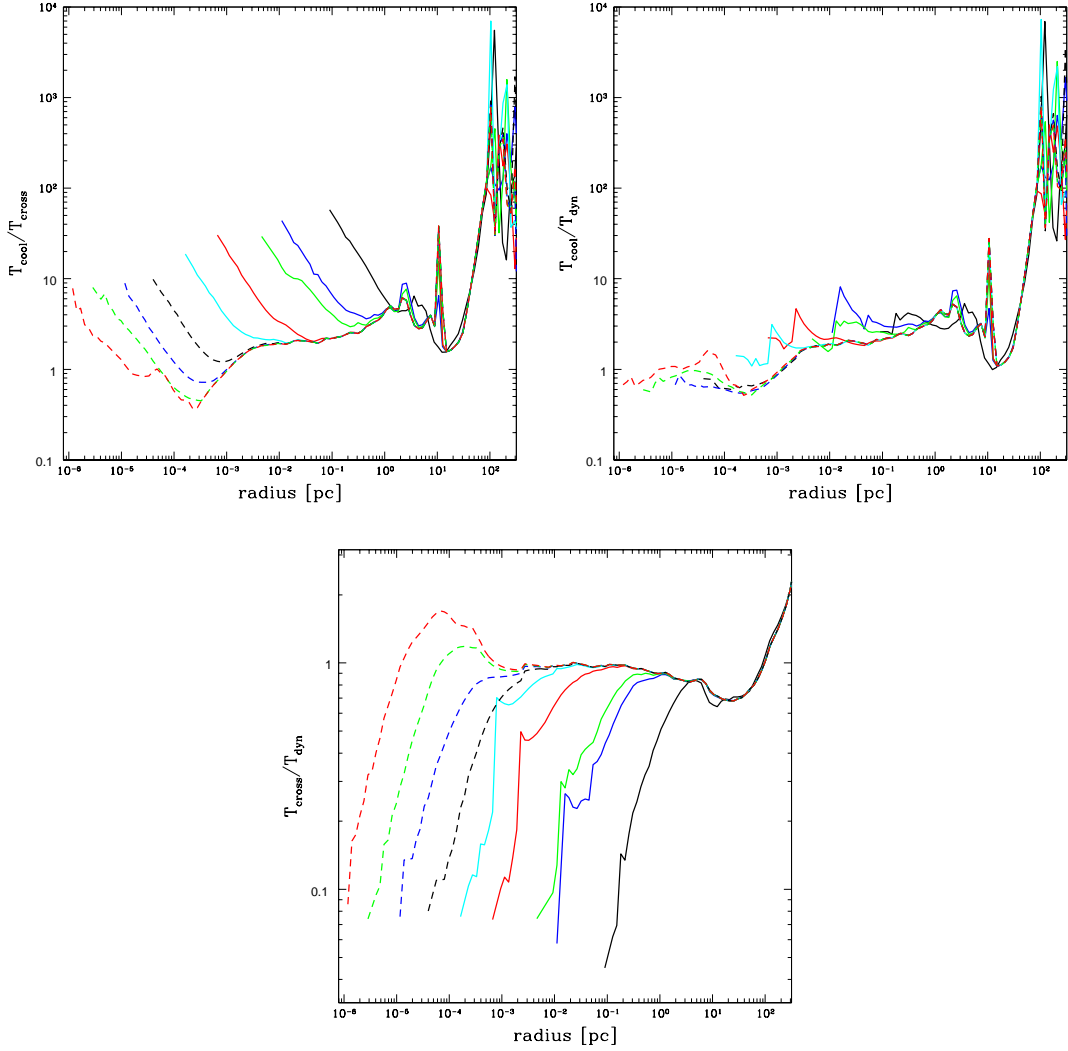
Figure 4.7: Evolution of the ratio of gas cooling time to sound crossing time (top left panel), gas cooling time to system dynamical time (top right panel), and sound crossing time to system dynamical time (bottom panel) as a function of radius of a representative primordial protostar. These quantities are mass-weighted and spherically-averaged, and the lines correspond to the same times as in Figure 4.4 and are of the same simulation.

at the speed of sound, resulting in the accretion rate described above. This accretion rate can be derived in a more intuitive way by considering the properties of a cloud of gas with radius R and mass M_{cl} which is marginally unstable. The accretion rate of this gas must be given (as an order of magnitude estimate) by $\dot{M} \sim M_{cl}/t_{dyn}$, where $t_{dyn} = R/a$, where a is the characteristic velocity associated with the cloud (the virial velocity). If this cloud was originally marginally supported against its self-gravity, then $a^2 \sim GM_{cl}/R$ (where G is the gravitational constant), which can be substituted into the expression for $\dot{M}$ to give $\dot{M} \sim a^3/G$, independent of R. In the case of this quasi-statically collapsing cloud, the virial speed is comparable to the sound speed c_s, giving $\dot{M} \sim c_s^3/G$. While the Shu model assumes that the entire cloud is of a constant temperature, our calculations have a varying temperature as a function of radius, and a radially-varying accretion rate based on this temperature is an excellent fit. This is reasonable because the isothermal collapse model assumes that the infall wave propagates at the local sound speed, assuming that the cloud is not supported by any other means. In this calculation we completely neglect the effects of magnetic fields, and it can be seen from Figure 4.6 that rotation contributes an insignificant amount of support, resulting in gas pressure being the sole means of support of the cloud.

Unfortunately, the final mass of the star remains unclear. This simulation (as well as all of the other calculations discussed in this chapter) lacks any of the necessary feedback processes that might halt accretion onto the protostar, making it impossible to accurately determine the main-sequence mass of the star. However, rough bounds on the mass of this object can be determined from examining Figure 4.8 and applying similar arguments to those used in ABN. A one solar mass protostar evolves far too slowly to halt accretion, particularly considering the high rates at which mass is falling onto the star ($\sim 10^{-2}$ $M_\odot$/year at $M_{enc} \leq 100$ $M_\odot$). Approximately 20 $M_\odot$ of gas will be accreted within 10^3 years, and ~ 60 $M_\odot$ of gas will be accreted within 10^4 years. A conservative minimum mass limit to this star should be approximately 20 $M_\odot$, since a thousand years is much shorter than the observed evolution timescales of galactic protostars. This is unclear, however, since little is known about the evolution of Population III protostars, whose evolution timescales may bear little relation to those of their modern-day brethren. A reasonable maximum mass is obtained by taking the mass at the maximum accretion time, which corresponds to $\sim 10^3$ $M_\odot$ at 2×10^6 years. However, the estimated main sequence lifetime of a ~ 300 $M_\odot$ primordial star is approximately 2×10^6 years, so it is implausible that the star could grow to be much larger than that. From these rough estimates, we obtain bounds on the mass of this Population III star of $\sim 20 - 300$ $M_\odot$. As discussed previously, however, this is a rough estimate at best – radiative feedback from the forming protostar will strongly affect the dynamics of the gas accreting onto the protostar. It is unlikely that photon pressure will significantly contribute to halting the accretion onto the protostar. However, as the star becomes luminous, production of ultraviolet light will cause photodissociation of molecular hydrogen in the accreting gas,

drastically affecting its cooling properties and possibly dramatically reducing or stopping the accretion of gas onto the protostar.

4.4.2 Angular momentum transport

One of the most pressing issues in modern-day star formation is the transport of angular momentum. The average rotational velocity observed in stars forming in the disk of our galaxy is several orders of magnitude smaller than one would assume if angular momentum of the collapsing molecular cloud out of which the star was formed were conserved, implying that somehow a huge amount angular momentum is transported away from the center of a collapsing molecular cloud core. The mechanisms responsible for this in the galaxy are generally believed to be the fragmentation of molecular cloud cores into multiple clumps (with the majority of the angular momentum going into their orbits around each other) and transport via magnetic fields.

The scenario with Population III stars is significantly different. Examination of the plot of radial velocity vs. radius in Figure 4.6 shows that the collapse of the cloud core is never stopped by rotational support. The reasons for this can be seen by the plot of angular momentum vs. enclosed gas mass in the same figure. At the onset of collapse, the core of the gas cloud has a very low specific angular momentum, with the overall distribution being generally well described by a power law. This is a natural consequence of dark matter halos which are produced by gravitational collapse, as explained by Quinn & Zurek [207], and is a result of efficient mixing and angular momentum transport during the relaxation of the halo. They show that for well-mixed halos the angular momentum distribution can be shown to have a power-law behavior, as is observed in this simulation. Examination of the halo in which the first protostar forms shows it to be well-mixed, with little substructure, and with the dark matter density profile of a halo in virial equilibrium. All of these clues suggest that one might expect the angular momentum distribution described above.

Even though the gas which ends up in the protostellar core starts out with very little angular momentum, it is clear from the plot of specific angular momentum vs. enclosed mass in Figure 4.6 that there is still some angular momentum transport occurring. This can be seen even more clearly in Figure 4.9, which shows the mean angular momentum evolution of the individual parcels of gas which end up at various radii in the dark matter halo which contains the first protostar. Due to the Eulerian nature of Enzo, we cannot in general directly follow the evolution of a specific parcel of gas. However, the code was modified to include "tracer particles," which are Lagrangian particles with zero mass that are placed in the baryon gas and simply follow along with the flow of the fluid. These particles were distributed evenly in the gas at the initialization of the simulation and were given unique numerical identifiers, allowing us to track each of their courses individually. These particles followed the flow of the baryon gas until the end of the simulation. At
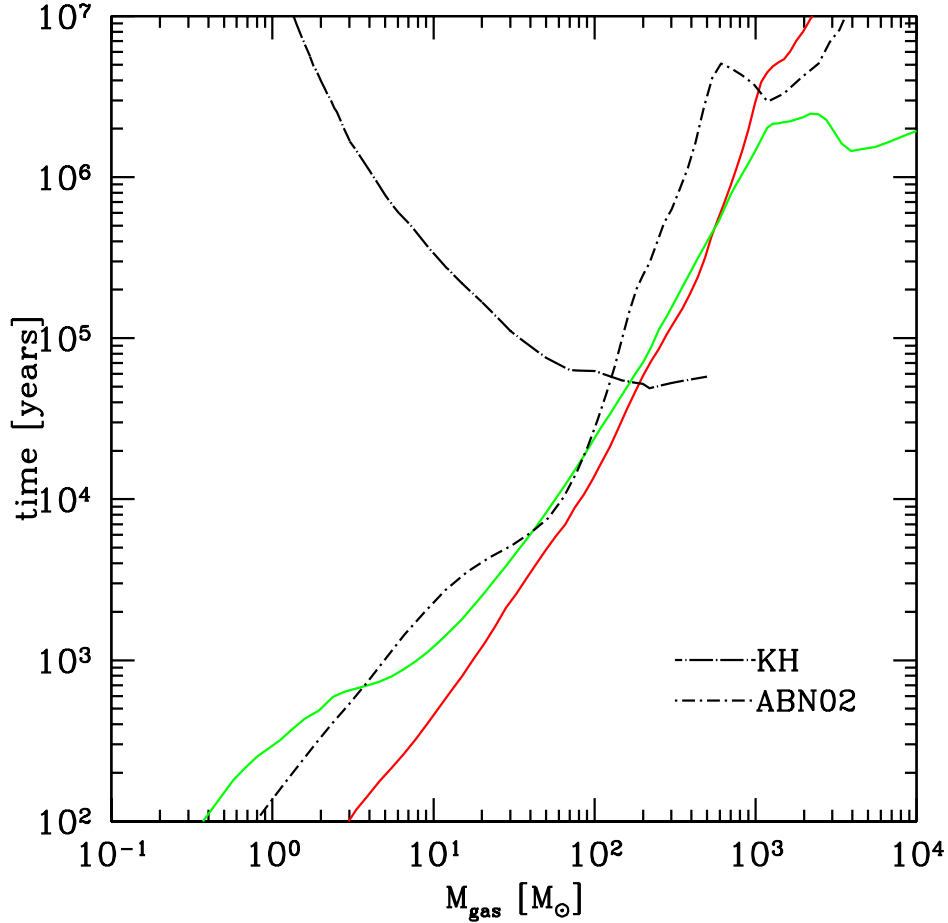
Figure 4.8: Baryon gas accretion time as a function of enclosed baryon mass for a representative primordial protostar. This is defined as $M_{enc}/\dot{M}$, where M_{enc} is the enclosed baryon mass and $\dot{M} \equiv 4\pi r^2 \rho(r) v(r)$, with $\rho(r)$ and $v(r)$ being the baryon density and velocity as a function of radius, and $v(r)$ defined as being positive towards the center of the halo. The red solid line is the baryon accretion time for this simulation. The green solid line is the accretion time as determined by taking the accretion rate from the Shu isothermal collapse model, $\dot{M}_{Shu} = m_0 c_s^3/G$, where m_0 is a dimensionless constant of order unity, c_s is the sound speed, and G is the gravitational constant. This value of $\dot{M}$ is calculated in each bin and the accretion time is plotted as $M_{enc}/\dot{M}_{Shu}$. The dot-long dashed line is the Kelvin-Helmholz time for a Population III star with a mass identical to the enclosed mass, as calculated from the results given by Schaerer. The dot-short dashed line is the baryon accretion time for the result in Abel, Bryan & Norman. The plot here corresponds to the last output dataset, corresponding to the red dashed line in Figures 4.4 through 4.7.

119

this time, we then bin the particles as a function of their final radius (separating the particles into bins spaced in roughly logarithmic intervals), and work backwards in time, calculating the mean angular momentum and radius of each bin of particles as a function of time. The results are displayed in the top panels of Figure 4.9. This shows that gas which is always outside of the core of the halo experiences proportionally very little transport of angular momentum or net movement inward, whereas the particles that end up in the innermost bins typically lose a factor of more than 50 in specific angular momentum and decrease their mean radius by a factor of more than 10. Figure 4.10 shows the evolution of cumulative angular momentum as a function of enclosed mass for this halo for each component of the angular momentum, as well as for the overall angular momentum of the system. This plot shows that the baryons within the cosmological halo conserve angular momentum overall. However, it is clear that within the innermost few thousand solar masses of gas, which corresponds to the quasistatically collapsing core of the halo, angular momentum is being redistributed outward.

What causes this transport of angular momentum? In this situation there are three plausible mechanisms for angular momentum transport in the absence of magnetic fields: Tidal coupling between gas in the core and the dark matter halo (or other nearby cosmological structures), non-axisymmetric perturbations in the baryons themselves (which generally serve to transport angular momentum outwards), and turbulent transport of angular momentum.

The first mechanism can be easily ruled out by examining the relative distributions of asymmetries in the baryons and dark matter. While the baryons that experience significant angular momentum transport show deviations from spherical symmetry on a scales of a few parsecs (see Figure 4.1), the dark matter is roughly spherical on scales smaller than 10 parsecs. This implies little tidal coupling between the two components of the halo. Tidal coupling from nearby cosmological structures can be ruled out by noting that the different components of the angular momentum appear to be redistributed in a similar manner, and also on a very rapid timescale. Tidal coupling from objects that are very far away and much larger than the halo core would cause relatively small changes which would take place much more gradually.

The analytical examination of non-axisymmetric perturbations requires us to treat the halo core as a disk. Using the formalism discussed by Hachisu et al. [208], we define a parameter $\beta \equiv T/|W|$, where T is the rotational energy and W is the gravitational energy, calculated in cylindrical shells around the axis of rotation. They show that an incompressible gas in axisymmetric equilibrium first experiences a dynamical gravitational instability that forms a non-axisymmetric perturbation (e.g. spiral density wave) at $\beta = 0.27$. The gas in our calculation is manifestly compressible, and Hachisu et al. show in a later paper that gas with a polytropic equation of state experiences these instabilities for $\beta \simeq 0.44$ [209]. The parameter β is calculated as a function of radius and shown in the top right panel of Figure 4.11 for the same series of simulation outputs
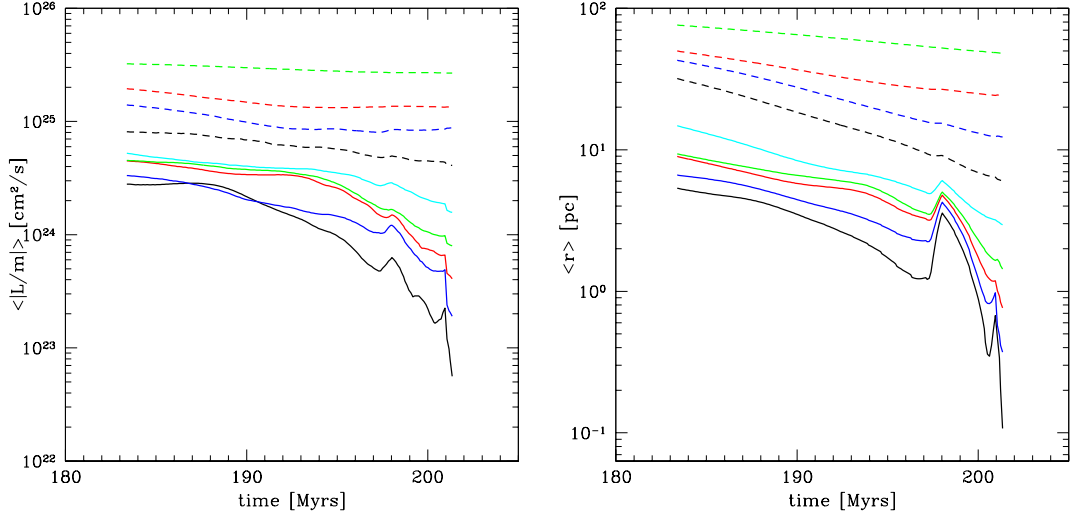
120

Figure 4.9: Evolution of mean baryon properties (as measured using baryon tracer parti-cles) as a function of time. Left: Mean particle specific angular momentum as a function of time. Right: Mean particle radius as a function of time. Each line corresponds to the mean quantity for a number of particles particles that are in a specific spherical shell at the end of the calculation, traced backwards through the simulation. Black solid line: all particles with $r_{part} \leq 0.25$ pc at the end of the simulation. Blue solid line: particles with $0.25 < r_{part} \leq 0.5$ pc. Red solid line:particles with $0.5 < r_{part} \leq 1$ pc. Green solid line: particles with $1 < r_{part} \leq 2$ pc. Cyan solid line: particles with $2 < r_{part} \leq 4$ pc. Black dashed line: particles with $4 < r_{part} \leq 8$ pc. Blue dashed line: particles with $8 < r_{part} \leq 16$ pc. Red dashed line: particles with $16 < r_{part} \leq 32$ pc. Green dashed line: particles with $32 < r_{part} \leq 64$ pc.
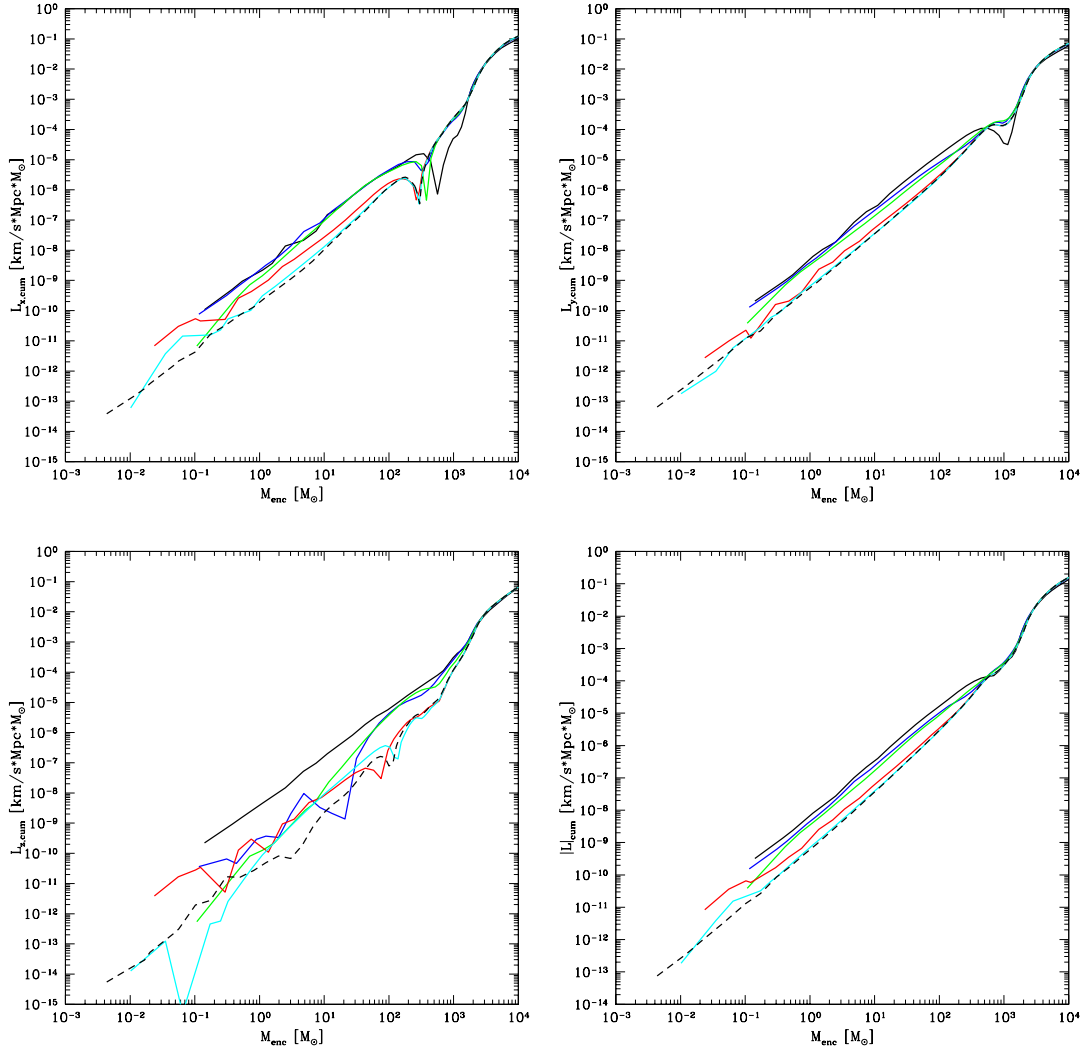
Figure 4.10: Cumulative angular momentum as a function of enclosed mass for several data outputs. Top left panel: absolute value of x component of angular momentum. Top right panel: absolute value of y component of angular momentum. Bottom left panel: absolute value of z component of angular momentum. Bottom right panel: total angular momentum. The lines correspond to the same times as in Figure 4.4 and are of the same simulation.

described in Section 4.4.1. The critical value of β for noncompressible and polytropic gases are shown as horizontal black lines. This plot shows that the only gas that could be susceptible to non-axisymmetric perturbations is at very large radii which, while it may experience some small amount of angular momentum transport over the the evolution of the halo, is at a distance where the overall rotational period of the gas is significantly longer than the the evolution time of the core of the halo. The beta values for the gas which is seen to be undergoing angular momentum transport are far too small for non-axisymmetric perturbations to be responsible for this transport. Additionally, visual inspection of the core of the halo does not show any sort of spiral arm-type structures which are the classical manifestation of non-axisymmetric perturbations.

One can analytically examine the turbulent transport of angular momentum in an accretion disk using the method described by Li et al. [210]. They show that the radial flux of the angular momentum can be calculated by integrating the off-axis component of the Reynolds stress tensor such that $F_L = < \Sigma \delta v_r \delta v_\phi >$, where F_L is the angular momentum flux, Σ is the surface density of the gas, $\delta v_r \equiv v_r - < v_r >$ is the deviation from the mean radial velocity, $\delta v_\phi \equiv v_\phi - < v_\phi >$ is the deviation from the mean circular velocity, and $< \ldots >$ indicates averaging over the azimuthal component, ϕ. The results are plotted in the bottom panel of Figure 4.11 in units of specific angular momentum transport (for consistency) and with line colors corresponding to previous plots in this chapter. A positive value of F_l indicates angular momentum transport outwards. There is some evidence for turbulent transport of angular momentum in this analysis.

One problem with the analytical results discussed above is that the approximation of a self-gravitating "thin disk" is very poor. Analysis of thin disks generally assumes that the scale height of the disk, h, is much smaller than the radius at any given point, r. The ratio of the scale height to the radius is typically calculated as $h/r \equiv c_s/v_{circ}$, where c_s is the sound speed and v_{circ} is the circular velocity. This implies that $c_s \ll v_{circ}$, which is not the case in this situation. In fact, for the radii in question, $c_s \simeq v_{circ}$, implying that the cloud core is spheroidal. This can be shown more quantitatively by examining the moment of inertia of the cloud core. The diagonal components of the moment of inertia have values that are similar. If the core were disk-like, one of the three components of the moment of inertia would be much smaller than the other two. Additionally, one cannot apply standard analytics that use a "thick disk" approximation because in standard situations where a thick disk is relevant, such as the accretion disks around compact objects, there is a central source (such as a black hole) whose gravity overwhelmingly dominates the self-gravity of the disk, which is not the case in this situation. Furthermore, analytical models of thin disks typically assume that the disk is rotating at a Keplerian orbital velocity (i.e. is rotationally supported) and that there is a central object such as a star or black hole dominating the gravitational potential. In the situation examined here, the overall circular velocity is far less than the Keplerian velocity and there is no central object dominating the potential. This casts further doubts on the validity of

using analysis techniques for thin disks on this particular situation.

Even though the validity of the analytical estimates for angular momentum transport discussed previously are dubious, this does not mean that all of the scenarios discussed previously are completely ruled out. Figure 4.13 shows the spherically-averaged, mass-weighted evolution of the radial velocity, RMS (root-mean-square) velocity of the baryon gas, and RMS Mach number of gas in the collapsing halo. Examination of this figure shows that at all radii where angular momentum transport is significant, the RMS velocity of the baryon gas is much greater than the average radial velocity, and that the average radial velocity is much smaller than the sound speed at most radii, while the RMS Mach number vs. radius plot shows that the baryon velocity is significantly larger than the sound speed at radii where angular momentum is being transported. This suggests that the gas in the core of the halo is experiencing significant supersonic turbulent motion, which may be responsible for the transport of angular momentum. In a turbulent medium in a gravitational potential, a given volume of space contains packets of gas that have a large distribution of angular momentum with respect to the center of the well. This turbulent medium effectively transports angular momentum outwards by allowing packets of gas with low angular momentum to sink towards the center of the potential well, replacing gas with higher angular momentum. This mechanism is only effective when the cooling time of the gas is longer than the dynamical time (e.g. when gas pressure plays a significant role). This scenario is given credibility by Figure 4.12, which shows a scatter plot of the specific angular momentum of tracer particles (with respect to the maximum baryon density) at the onset of halo collapse to the distance of that particle from the baryon density maxima at the point at which the simulation is terminated. Gas within the innermost few parsecs (which is the region undergoing quasistatic collapse and angular momentum transport) shows a distinct (though noisy) relationship between initial angular momentum and final distance with respect to the halo center.

A further possible source of transport of angular momentum could be due to numerical shear viscosity. In order to determine whether this is the case, a parameter study was carried out where we varied the effective resolution of the simulation by a factor of 16 along each grid axis by enforcing that the Jeans length be resolved by a minimum of 4, 16 or 64 cells. The properties of the halo in all cases were very similar. Additionally, we used two different hydrodynamical methods (both PPM and the method used in the ZEUS code) with different orders of accuracy, and found no significant differences between the two calculations. The ZEUS hydro method has an explicit artificial viscosity for shock capturing purposes, and the PPM method uses a Riemann solver which has no explicit numerical viscosity, and they get the same result. While this is not a formal proof of the lack importance of numerical viscosity, it is highly suggestive that the observed angular momentum transport is not caused by numerical effects.

Quantifying the magnitude of numerical viscosity is difficult due to the range of spatial and temporal resolutions. The most straightforward way to do so would be to simulate
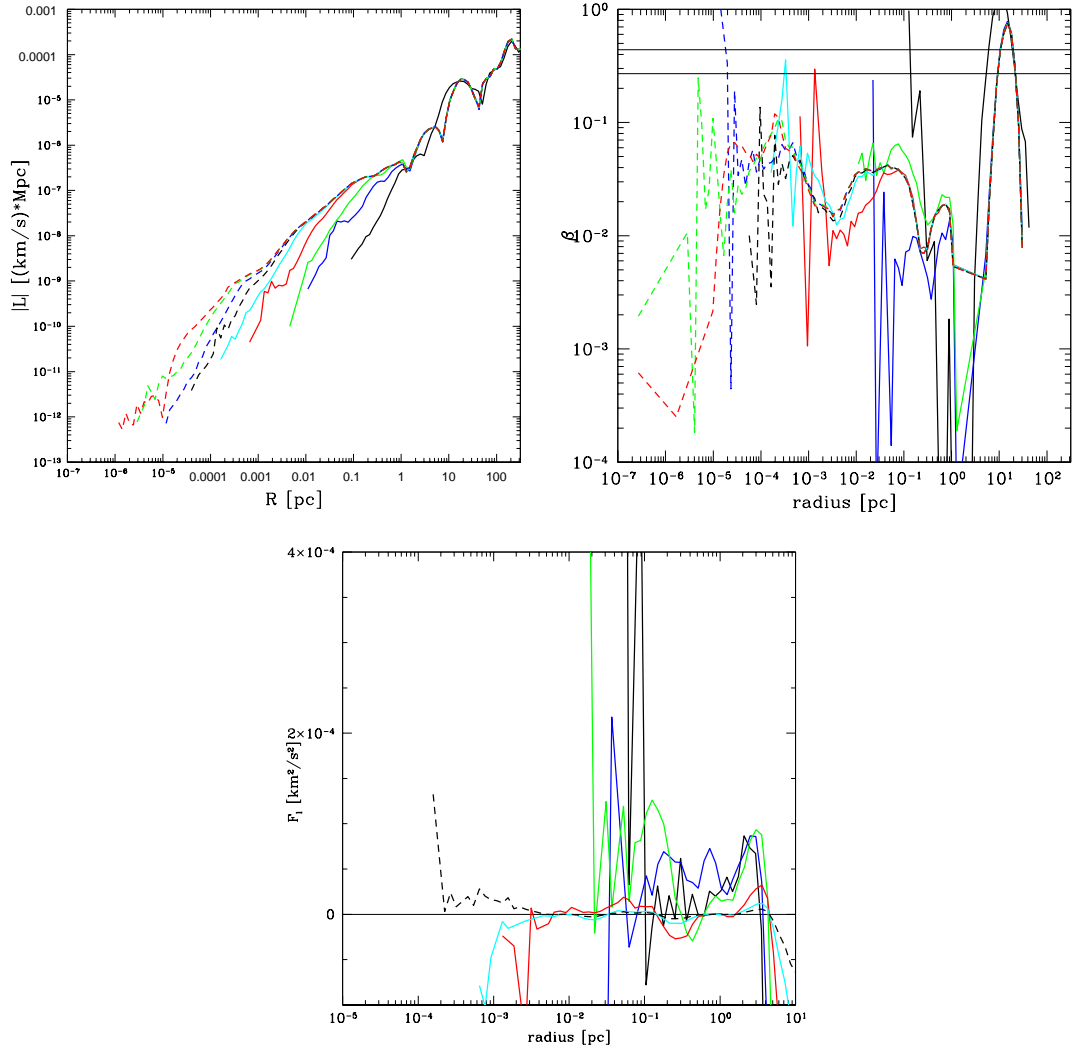
Figure 4.11: Evolution of quantities related to the angular momentum as a function of radius at several output times. Top left panel: Specific angular momentum as a function of radius. Top right panel: Evolution of the β parameter as a function of radius. Bottom panel: specific angular momentum flux as a function of radius. In the top right panel the critical values of β for compressible and noncompressible fluids are shown by the top and bottom horizontal black lines, respectively. The line colors correspond to the same output times as are described in previous figures.

125
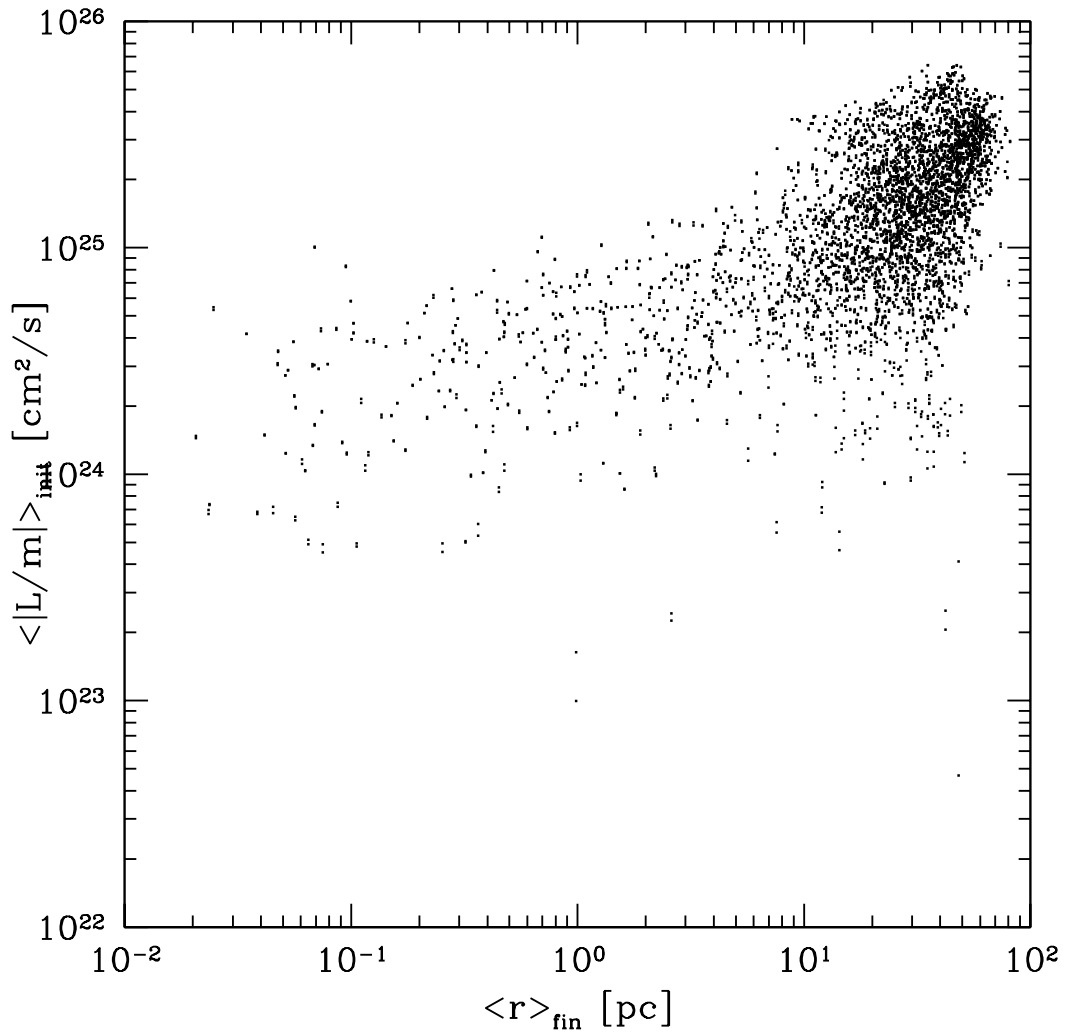
Figure 4.12: Scatter plot of initial specific angular momentum of tracer particles with respect to the maximum density of the collapsing halo core versus the particle's final distance from the halo core at the point that the simulation is terminated.

a problem with an analytical solution that explicitly includes viscosity and solve it on an adaptive grid using the Euler equations, which implicitly assume no viscosity. Then one would observe the evolution of the problem and post facto estimate the numerical viscosity. The numerical viscosity in an adaptive mesh code may be highly dependent on the test problem.

4.4.3   Consistency of result across multiple realizations

Another important issue relating to studies of the formation of Population III stars in a cosmological context is the consistency of the results over a range of simulation parameters. As discussed in Section 4.2, previously published high dynamical range calculations of Pop III star formation have concentrated upon a single cosmological realization. While this is an important first step, it neglects possible systematic effects relating to simulation box size and other parameters, and also allows for error due to small number statistics.

In this section I attempt to address some of these issues. Twelve simulations are set up as described in Section 4.3. Each simulation has a different cosmological realization (i.e. large scale structure). Four simulations in each of three box sizes ($0.3, 0.45$, and 0.6 h^{-1} comoving Mpc) are performed, with the results shown in Figures 4.14 through 4.23.

Figures 4.14 - 4.16 display several mean properties of the halos. In each of the panels in these graphs the information for each separate simulation is plotted as a filled-in square which is color coded according to box size as described in the figure captions. The colored crosses correspond to mean values for all simulations of a given box size (with colors again corresponding to the box size), and the green circle corresponds to the mean of all twelve of the simulations together.

The top left panel of Figure 4.14 shows the virial mass of each halo at the time of protostellar cloud collapse plotted against the redshift of collapse. Though there is a large amount of scatter in virial mass overall (with the smallest halo having a mass of 1.36×10^5 M$_\odot$ and the largest 6.92×10^5), the average virial mass in each box size is virtually identical. The mean virial mass of all twelve of the halos is 3.63×10^5 M$_\odot$, which is significantly lower than the halo mass of 7×10^5 M$_\odot$ in ABN. In contrast to the virial mass, there is a strong trend in earlier collapse time (large collapse redshift) as a function of box size, with the 0.45 and 0.6 h^{-1} Mpc boxes collapsing at a mean redshift of $z \simeq 27.5$ and the 0.3 h^{-1} Mpc boxes collapsing at a mean redshift of $z \simeq 22$. This can be understood as a result of the distribution of power as a function of simulation volume. Since the power as a function of wave number falls off as $P(k) \sim k^{-3}$ at large wave numbers (small box sizes), doubling the box size significantly increases the power on large scales. The net results of this is that the most massive halo in each box forms significantly earlier, out of a density peak that is statistically denser overall, and also undergoes a more rapid merger history. An effect of this can be seen in the top
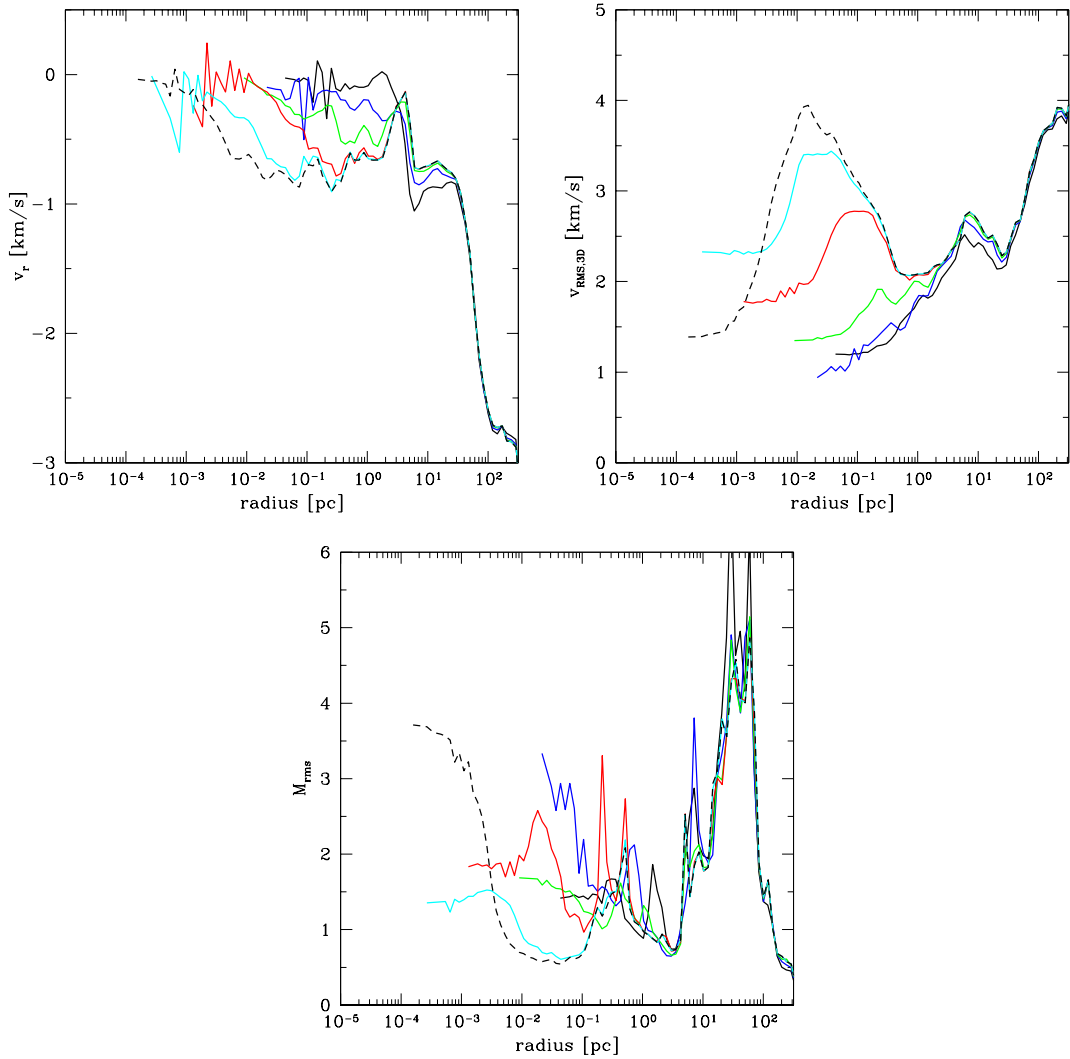
Figure 4.13: Top left panel: spherically-averaged, mass-weighted radial velocity as a function of radius for several simulation output times. Top right panel: spherically-averaged, mass-weighted root-mean-square velocity as a function of radius for several simulation output times. Bottom panel: spherically-averaged, mass-weighted RMS Mach number as a function of radius for several simulation output times. The line colors correspond to the same output times as are described in previous figures.

right panel of Figure 4.14, which shows the mean baryon temperature in each halo as a function of collapse redshift. As with the plot of virial mass vs. collapse redshift, there is a significant amount of scatter in the results, but a clear trend of increased overall halo temperature with box size is apparent. This is explainable in terms of competing heating and cooling effects. The gas in a given halo is heated by shocking during merger events, and cools radiatively (primarily due to line cooling from molecular hydrogen at these temperatures for a gas of primordial composition). A higher overall merger rate results in a warmer overall halo temperature assuming that the halo merger rate is comparable to the overall gas cooling rate (which is true for halos in the early universe). However, the rate of molecular hydrogen production at low densities increases as a function of temperature (due to the increased availability of free electrons) at the temperatures relevant to Population III halos, so even though the halos that form in larger boxes have higher overall mean temperatures, they also produce more molecular hydrogen in their cores, leading to an overall cooler halo core when collapse takes place. This will be discussed in more detail later in this section.

The mean halo baryon temperature vs. halo virial mass is plotted in the bottom left panel of Figure 4.14, and the mean halo temperature versus the halo virial temperature is plotted in the bottom right hand panel. The dashed line in the plot of halo mean temperature vs. virial mass scales as $T \sim M^{2/3}$, arbitrarily scaled to intersect the mean temperature and mass value for all simulations. This is the scaling relation expected from gas in a halo forming in a situation where radiative cooling is unimportant, and is commonly used to understand the mass-temperature relationship of the intracluster medium in galaxy clusters. There is some relationship between mean temperature and virial mass that generally conforms to this power law, which is due to the relatively poor cooling properties of molecular hydrogen. Still, there is a great deal of scatter in the relationship. The amount of scatter is reduced when considering the mean halo temperature vs. halo virial radius (shown in the bottom right hand panel). The halo virial temperature is a function of both halo mass and of redshift, with $T_{vir} \sim M_{vir}^{2/3}(1+z)$. The reduction in scatter is primarily due to the general trend of halos collapsing at higher redshifts having higher overall gas temperatures for an unevolving mean virial mass, which results in overall higher virial temperatures at high redshift. Though there is a clear relationship between halo baryon temperature and virial temperature, the mean baryon temperature in all cases is significantly lower than the halo virial temperature, suggesting that radiative cooling plays a non-negligible role in the overall temperature of the halo despite its generally poor cooling properties at low temperatures. If radiative cooling were completely unimportant the mean halo baryon temperature would be approximately the virial temperature.

Figure 4.15 shows the relationship of the angular momentum in the halos with various quantities. The angular momentum of a cosmological halo can be described as a function of the dimensionless spin parameter, $\lambda \equiv J|E|^{1/2}/GM^{5/2}$, where J is angular momentum,
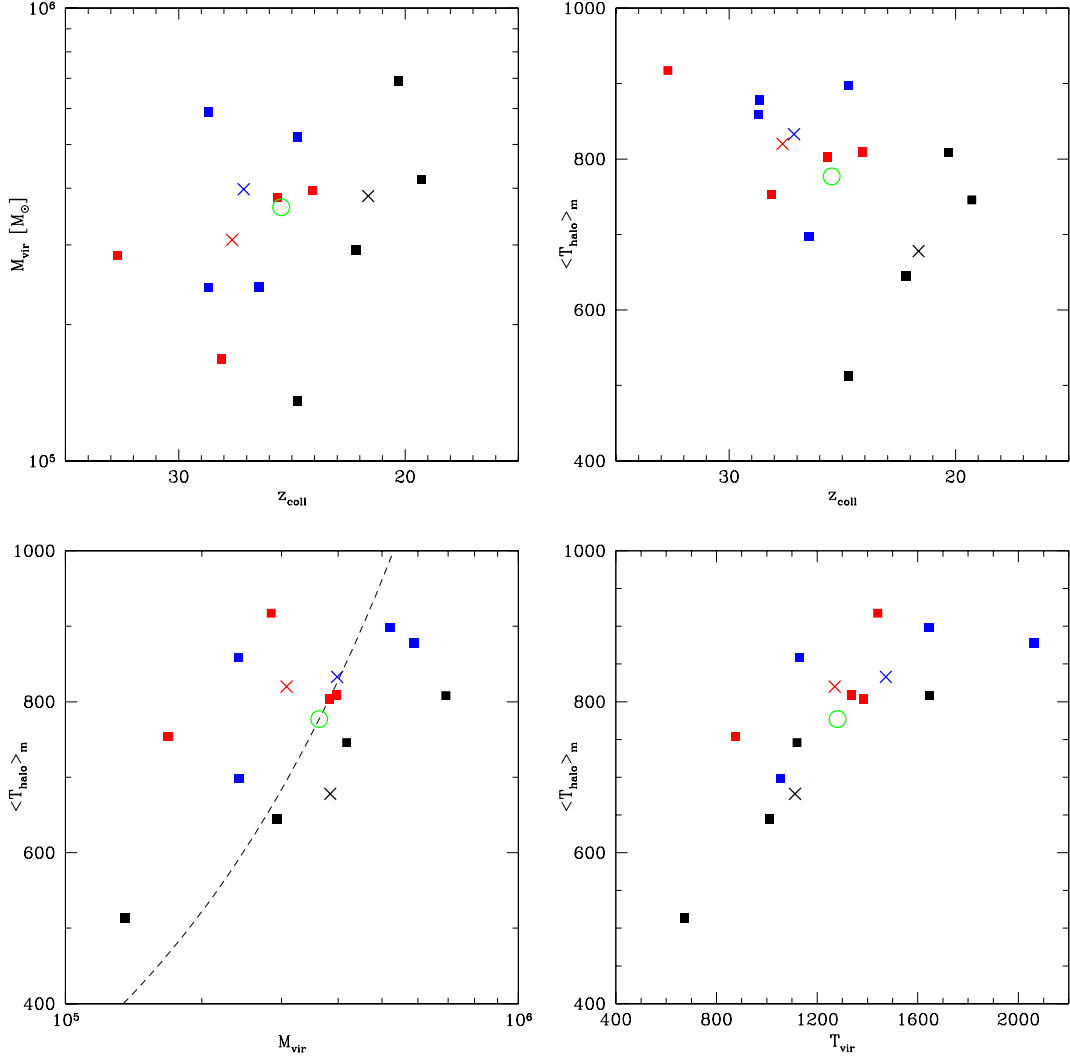
Figure 4.14: Plots of basic halo quantities for 12 different cosmological random realizations. Top left panel: halo virial mass vs. protostar collapse redshift. Top right panel: mean mass-weighted halo baryon temperature vs. collapse redshift. Bottom left panel: mean mass-weighted halo vs. halo virial mass. Bottom right panel: halo mean baryon temperature vs. halo virial temperature. In each plot, black, blue and red squares correspond to simulations with 0.3 h^{-1} Mpc, 0.45 h^{-1} Mpc and 0.6 h^{-1} Mpc comoving box sizes. Each colored "x" corresponds to the average value for simulations with that box size, with colors corresponding to the same simulation box sizes as the squares. The green circle corresponds to the average for all simulations together. The dashed line in the plot of halo mean temperature vs. virial mass (bottom left) scales as $T \sim M^{2/3}$, arbitrarily scaled to intersect the mean temperature and mass value for all simulations.

E is the total energy, G is the gravitational constant and M is the halo mass. This is roughly equivalent to the ratio of the angular momentum of the halo to the angular momentum needed for the halo to be rotationally supported. Typical values for the halo spin parameter are $0.02-0.1$, with a mean value of 0.05 [221, 222]. The gas spin parameter is somewhat lower than the dark matter spin parameter, which this is a function of the way in which the total energy and masses are calculated, and not an indication that there is less angular momentum per unit mass in the baryons as opposed to the dark matter.

The top left panel of Figure 4.15 shows the gas and dark matter spin parameters plotted against each other for the halo in each simulation that forms the Population III protostar, at the time of collapse. The mean value of the dark matter spin parameter is approximately 0.05, and both this and the overall range and distribution of the spin parameters agree with previous analytical and numerical results [221, 222]. The baryon gas spin parameter is lower overall (this is an effect of the scaling of the parameter and should be taken as a renormalization), and the distribution agrees with previous work. There appears to be some overall positive correlation between the dark matter and baryon spin parameters (e.g. halos with higher overall dark matter angular momentum tend to have higher overall baryon angular momentum) but there is considerable scatter. In all cases the spin parameters are much less than one, which suggests that the halos have little overall angular momentum. This is a general property of cosmological halos, and is consistent with previous analytical and numerical work, as well as the properties of angular momentum in the representative halo discussed in Section 4.4.1.

The top right hand panel of Figure 4.15 plots dark matter spin parameter vs. collapse redshift of the halo. There is no evidence for evolution of the spin parameter with redshift. The bottom left and right panels of Figure 4.15 plot the baryon and dark matter spin parameters against the halo virial mass. As with the other quantities examined, there is considerable scatter in the distributions, but no evidence for a clear relationship between halo virial mass and either gas or dark matter spin parameter. In all of the panels of this figure there is no evidence for any systematic effect due to box size.

Figure 4.16 plots the angle between the overall dark matter and baryon angular momentum vectors (θ) versus several different quantities. The top left panel plots θ vs. halo virial mass at the time of formation of the Pop III protostar in each halo. Overall, the average value for θ is approximately 25 degrees, which is consistent with recent numerical simulations. There is a great deal of scatter in θ, which is also consistent. There is no evidence for correlation between θ and halo virial mass. The top right panel plots θ vs. collapse redshift for each simulation, and the bottom left and right panels plot the gas and dark matter spin parameters vs. θ, respectively. There appears to be no correlation between θ and collapse redshift or the gas or dark matter spin parameters, and no evidence of there being any systematic effect due to box size.

In addition to plots of mean halo properties, it is very useful to look at more detailed information about each halo. Figures 4.17 through 4.23 show spherically-averaged, mass-
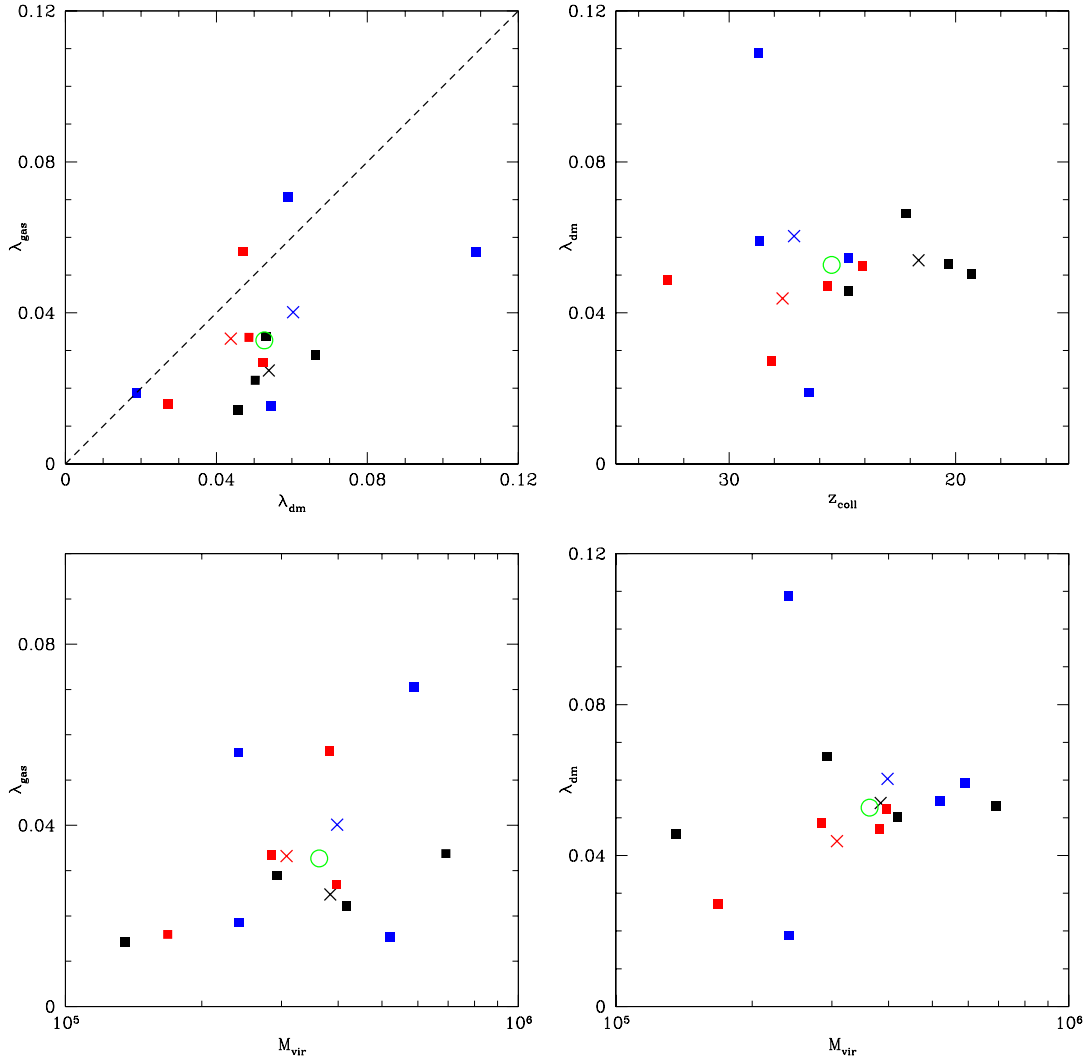
Figure 4.15: Plots of basic halo quantities for 12 different cosmological random realizations. Top left panel: gas spin parameter vs. dark matter spin parameter. Top right panel: dark matter spin parameter vs. halo collapse redshift. Bottom left: gas spin parameter vs. halo virial mass. Bottom right: dark matter spin parameter vs. halo virial mass. In each plot, black, blue and red squares correspond to simulations with 0.3 h^{-1} Mpc, 0.45 h^{-1} Mpc and 0.6 h^{-1} Mpc comoving box sizes. Each colored "x" corresponds to the average value for simulations with that box size, with colors corresponding to the same simulation box sizes as the squares. The green circle corresponds to the average for all simulations together.
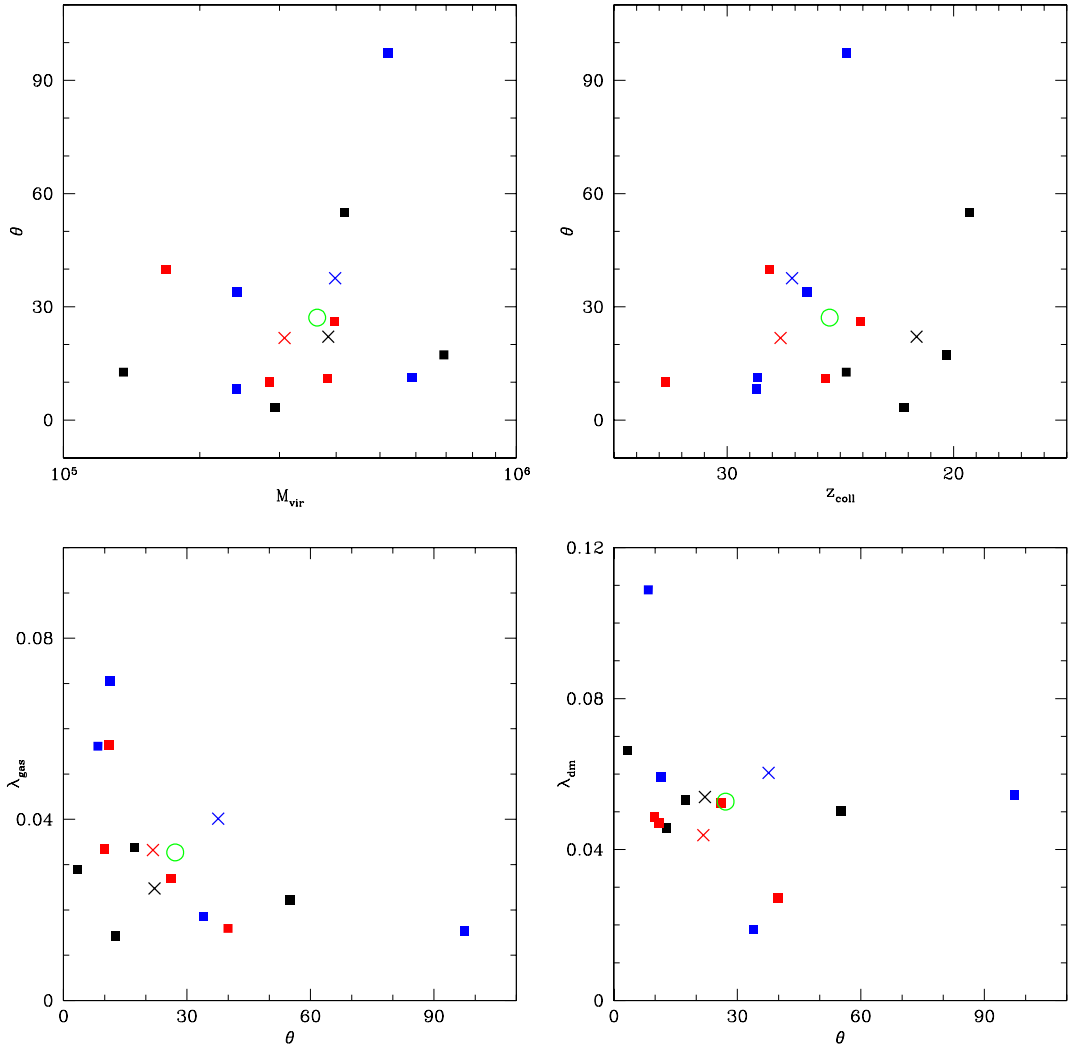
Figure 4.16: Plots of basic halo quantities for 12 different cosmological random realizations. Top left panel: Theta (angle between gas and dark matter angular momentum vectors) vs. halo virial mass. Top right panel: theta vs. halo collapse redshift. Bottom left panel: gas spin parameter vs. theta. Bottom right panel: dark matter spin parameter vs. redshift. In each plot, black, blue and red squares correspond to simulations with 0.3 h^{-1} Mpc, 0.45 h^{-1} Mpc and 0.6 h^{-1} Mpc comoving box sizes. Each colored "x" corresponds to the average value for simulations with that box size, with colors corresponding to the same simulation box sizes as the squares. The green circle corresponds to the average for all simulations together.

weighted radial profiles of several baryon quantities in eleven of the twelve simulations (one simulation crashed and could not be restarted before reaching a high enough density). Since the cores of the most massive halo in each simulation collapse at a range of redshifts, it is not worthwhile to compare each halo at a specific point in time. Instead, we choose to compare them at a fixed point in the halo's evolution, as measured by the peak central baryon density in the protostellar cloud, which is roughly analogous to a constant point in the evolution of the protostar. In each of the figures discussed below, the top left panel shows radial profiles for all of the simulations plotted together. The top right panel shows only the results for the 0.3 h^{-1} Mpc box, the bottom left panel shows only results for the 0.45 h^{-1} Mpc box, and the bottom right panel shows only results for the 0.6 h^{-1} Mpc box. Line of a given color and line type correspond to the same simulation in all figures.

Figure 4.17 shows the plots of number density as a function of radius for eleven simulations, shown at approximately the same point in their evolution. There is remarkably little scatter in the density profiles for all of the simulations, and the density profiles all tend towards $\rho(r) \sim r^{-2}$. It was shown by Bodenheimer & Sweigart [205] that for a cloud of gas that is nearly isothermal and slowly rotating and which has negligible support from a magnetic field, the subsonic evolution of the gas will tend to produce a $1/r^2$ density distribution as long as the thermal pressure remains approximately in balance with the gravitational field. In particular, Chandrasekhar [206] showed that a molecular cloud core which forms at subsonic speeds will tend towards the density distribution of a singular isothermal sphere,

$$\rho(r) = \frac{c_s^2}{2\pi G r^2} \tag{4.1}$$

where $c_s \equiv (kT/m)^{1/2}$ is the isothermal sound speed, T, k, and m are the temperature, Boltzmann's constant, and mean molecular weight of the gas, respectively, and and r is the radius. Since the halos generally have low angular momentum (as seen in Figure 4.15) and magnetic fields are completely neglected in these simulations, it is reasonable that the density go as $\rho(r) \sim r^{-2}$ in all of the simulations. The overall normalization of the density profiles also agrees very well. This can be understood as a result of the cooling properties of hydrogen gas. Each of the halos examined in this figure has the same composition, and therefore is cooled by the same mechanism. Only a small amount of molecular hydrogen is needed to cool the gas relatively efficiently, suggesting that in a halo that is in a somewhat stable equilibrium the gas temperature at low densities should be approximately constant for different halos, independent of the molecular hydrogen fraction. At densities above approximately 10^4 cm^{-3} the cooling rate becomes independent of density and the overall evolution of the gas happens very rapidly, so small differences in the initial molecular hydrogen fraction become magnified (as discussed later in this section).
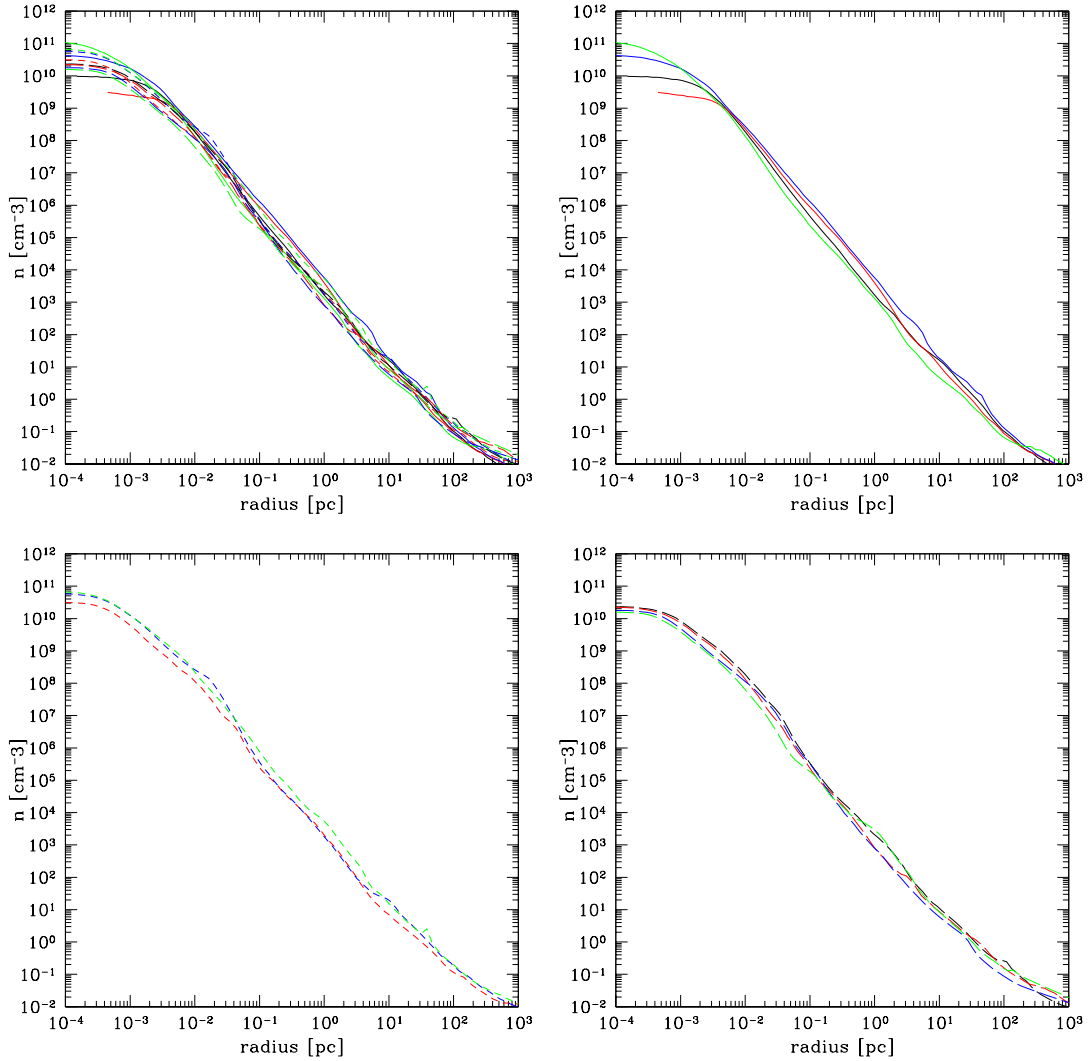
Figure 4.17: Mass weighted, spherically-averaged baryon number density as a function of radius for 11 different cosmological random realizations, chosen at an output time where peak baryon density values are approximately the same. There are three box sizes: 0.3 h^{-1} Mpc, 0.45 h^{-1} Mpc and 0.6 h^{-1} Mpc (comoving). One of the 0.45 h^{-1} Mpc simulations has been omitted since the simulation crashed before reaching a comparable density value. Top left panel: All 11 simulations plotted together. Top right panel: 0.3 h^{-1} Mpc box simulations. Bottom left panel: 0.45 h^{-1} Mpc box simulations. Bottom right panel: 0.6 h^{-1} Mpc box simulations.

Figure 4.18 shows the baryon temperature as a function of radius. At radii outside of ~ 1 parsec, the temperature profiles are similar between all of the simulations, though halos forming in larger simulation volumes tend to have a higher overall temperature. At smaller radii there is significant scatter in core temperature of the simulations (for a fixed density), with a systematic trend towards halos forming in larger boxes having a lower overall core temperature. Examination of Figure 4.19 (molecular hydrogen mass fraction as a function of radius) shows that halos which form in a larger simulation volume have systematically larger H_2 mass fractions, though this effect is much more pronounced in the core of the halo than in the envelope. This difference in molecular hydrogen fraction can be understood as a result of the overall halo temperature. The rate at which molecular hydrogen is produced at low densities is limited by the availability of free electrons, as described in Section 1.3.2. The mean fraction of free electrons available in the primordial gas is a function of baryon temperature, with larger temperatures corresponding to larger electron fractions. On the other hand, the rate at which molecular hydrogen forms via the H^- channel declines at high temperatures. Since the limiting reaction in the formation of molecular hydrogen via the H^- channel is the formation of free electrons, this reaction dominates, and it can be shown using a simple one-zone calculation following the nonequilibrium primordial chemistry that molecular hydrogen production is maximized at ~ 1000 K. Halos with higher overall baryon temperatures will have systematically higher molecular hydrogen fractions. Once the core of the halo begins to collapse to very high densities small differences in the molecular hydrogen fraction are amplified, resulting in a general trend towards halos with higher overall baryon temperatures having higher H_2 fractions in their cores, and thus lower central temperatures.

Figures 4.20 and 4.21 show the enclosed baryon mass and circular velocity in each halo as a function of radius. The plot of enclosed mass versus radius shows very little scatter between the different simulations. This is to be expected since this is essentially another way of showing that the overall density distributions of the halos has little scatter (as in Figure 4.17), and is a result of the cooling properties of a primordial gas. The plot of circular velocity as a function of radius shows much more scatter, though there is no clear trend with simulation box size. In all cases the overall circular velocity is significantly less than the Keplerian orbital velocity, which agrees with our previous observation that the halos have generally low angular momentum, and that during the collapse of the core angular momentum is transported outward by turbulence.

It is useful to examine Figures 4.22 and 4.23 together, since they are essentially two different ways of looking at the same data. Figure 4.22 is the mean baryon radial velocity as a function of radius, and Figure 4.23 is the baryon accretion time as a function of enclosed mass. Figure 4.22 shows that there is a clear systematic effect present, where halos forming in simulations with larger boxes having a significantly lower overall radial velocity at small radii. This translates directly to a lower overall accretion rate
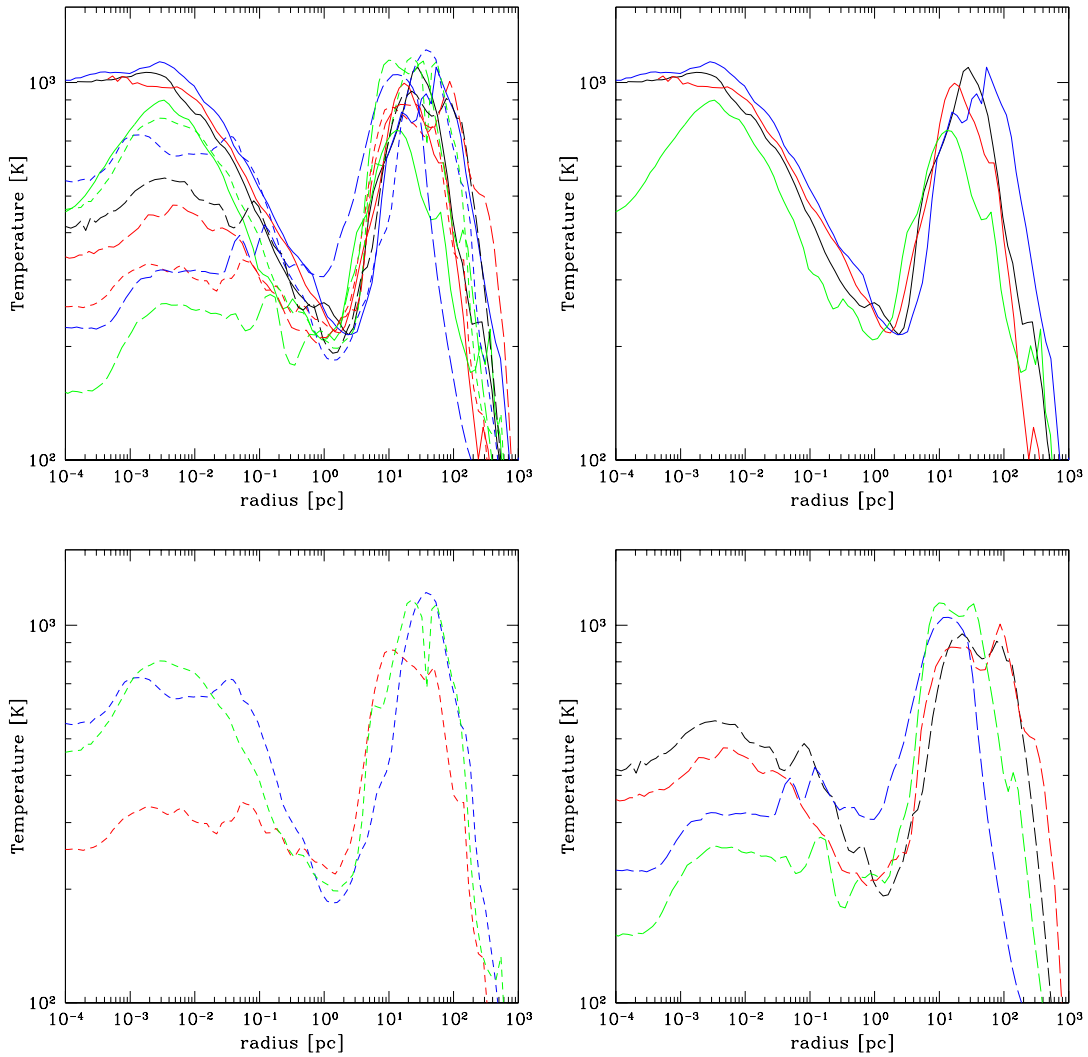
Figure 4.18: Mass-weighted, spherically-averaged baryon temperature as a function of radius for 11 different cosmological random realizations, chosen at an output time where peak baryon density values are approximately the same. There are three box sizes: 0.3 h^{-1} Mpc, 0.45 h^{-1} Mpc and 0.6 h^{-1} Mpc (comoving). One of the 0.45 h^{-1} Mpc simulations has been omitted since the simulation crashed before reaching a comparable density value. Top left panel: All 11 simulations plotted together. Top right panel: 0.3 h^{-1} Mpc box simulations. Bottom left panel: 0.45 h^{-1} Mpc box simulations. Bottom right panel: 0.6 h^{-1} Mpc box simulations.
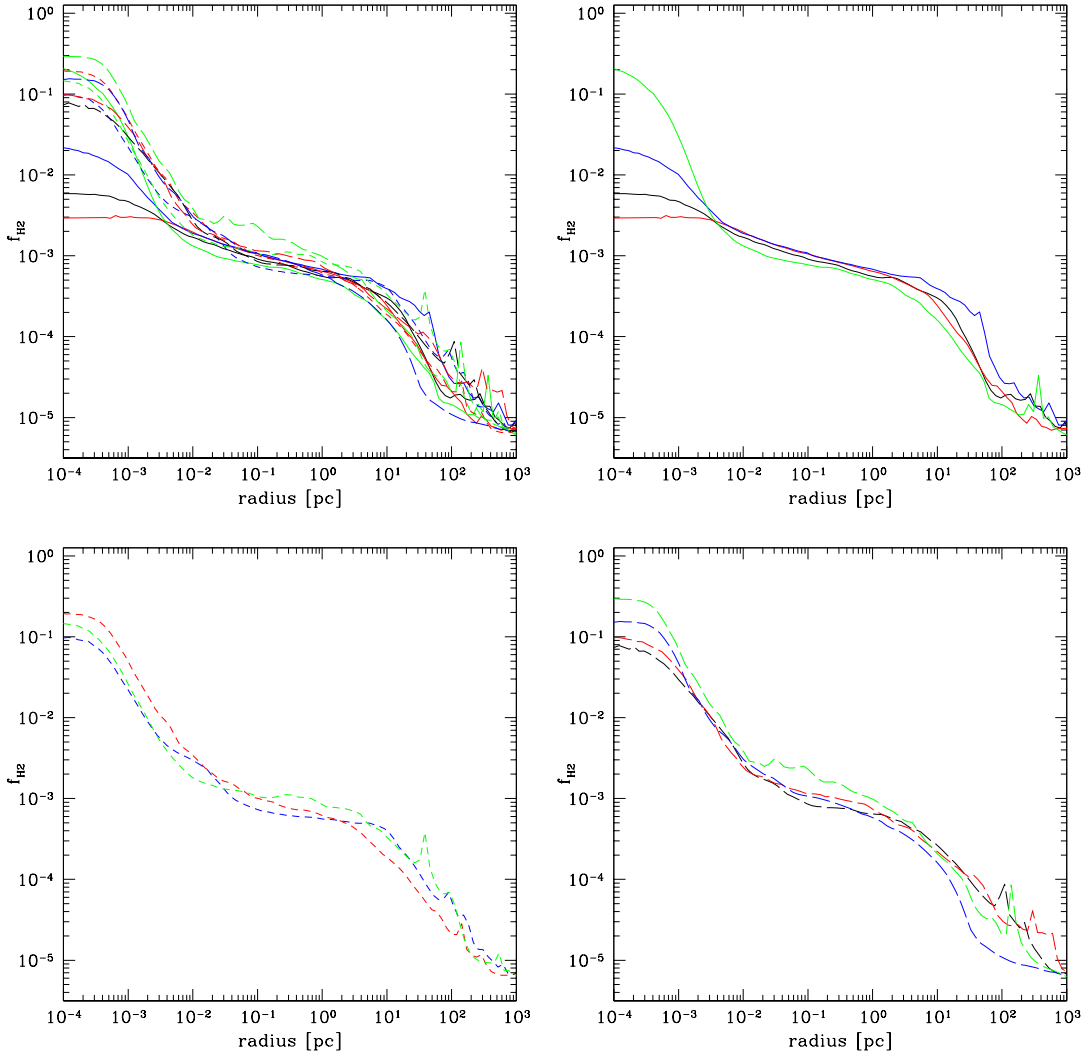
Figure 4.19: Mass-weighted, spherically-averaged molecular hydrogen fraction as a function of radius for 11 different cosmological random realizations, chosen at an output time where peak baryon density values are approximately the same. There are three box sizes: 0.3 h^{-1} Mpc, 0.45 h^{-1} Mpc and 0.6 h^{-1} Mpc (comoving). One of the 0.45 h^{-1} Mpc simulations has been omitted since the simulation crashed before reaching a comparable density value. Top left panel: All 11 simulations plotted together. Top right panel: 0.3 h^{-1} Mpc box simulations. Bottom left panel: 0.45 h^{-1} Mpc box simulations. Bottom right panel: 0.6 h^{-1} Mpc box simulations.
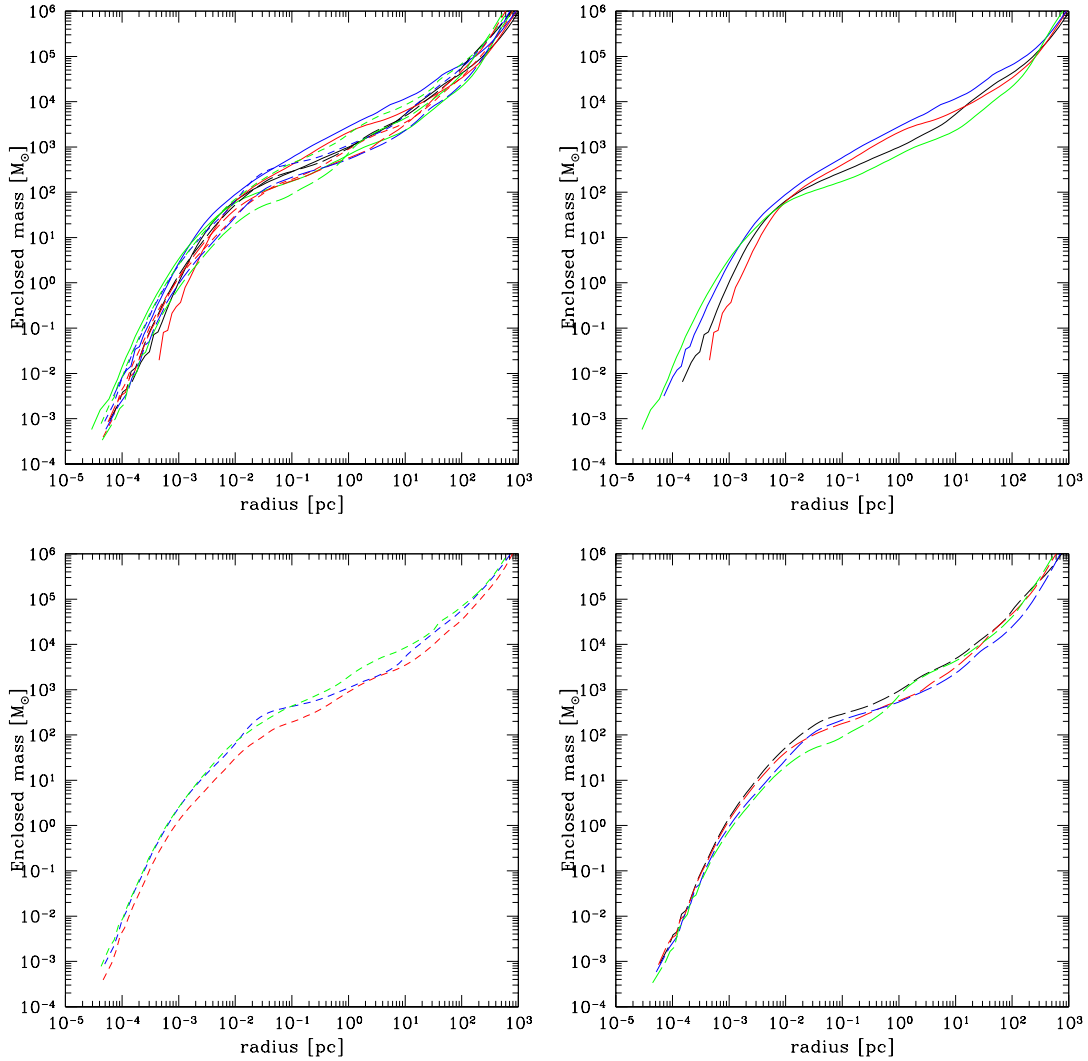
Figure 4.20: Mass-weighted, spherically-averaged enclosed baryon mass as a function of radius for 11 different cosmological random realizations, chosen at an output time where peak baryon density values are approximately the same. There are three box sizes: 0.3 h^{-1} Mpc, 0.45 h^{-1} Mpc and 0.6 h^{-1} Mpc (comoving). One of the 0.45 h^{-1} Mpc simulations has been omitted since the simulation crashed before reaching a comparable density value. Top left panel: All 11 simulations plotted together. Top right panel: 0.3 h^{-1} Mpc box simulations. Bottom left panel: 0.45 h^{-1} Mpc box simulations. Bottom right panel: 0.6 h^{-1} Mpc box simulations.
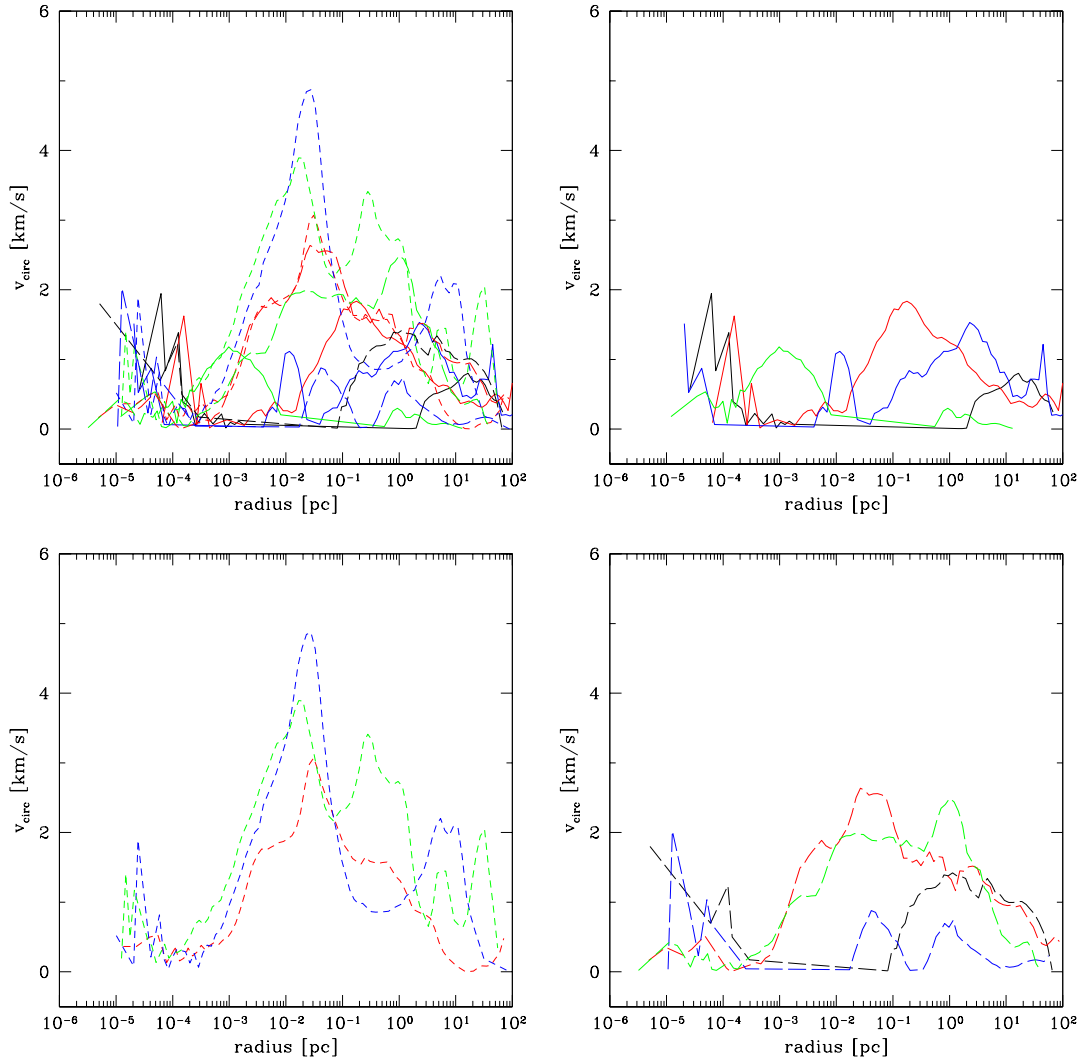
139

Figure 4.21: Mass-weighted, cylindrically-averaged baryon circular velocity as a function of radius for 11 different cosmological random realizations, chosen at an output time where peak baryon density values are approximately the same. There are three box sizes: $0.3 \ h^{-1}$ Mpc, $0.45 \ h^{-1}$ Mpc and $0.6 \ h^{-1}$ Mpc (comoving). One of the $0.45 \ h^{-1}$ Mpc simulations has been omitted since the simulation crashed before reaching a comparable density value. Top left panel: All 11 simulations plotted together. Top right panel: $0.3 \ h^{-1}$ Mpc box simulations. Bottom left panel: $0.45 \ h^{-1}$ Mpc box simulations. Bottom right panel: $0.6 \ h^{-1}$ Mpc box simulations.

onto protostellar forming in halos in larger simulation volumes, which can be seen in Figure 4.23. For a wide range of enclosed mass, the average accretion rate of halos in the $0.6 \ h^{-1}$ Mpc simulations is more than an order of magnitude less than that of halos in the $0.3 \ h^{-1}$ Mpc boxes. As discussed in Section 4.4.1, this can be understood using the Shu isothermal sphere model, where subsonic collapse of gas onto the core of the sphere occurs at a rate controlled by the sound speed. Since the core temperatures are lower overall in the large simulation volumes, this translates to a lower sound speed and overall lower accretion rate. The implications of this are extremely significant – a lower accretion rate implies a lower overall Population III IMF in larger boxes. Applying the same estimates for the bounds of the stellar masses used in Section 4.4.1, we obtain a mass range of roughly $10 - 500 \ M_\odot$ for all four of the halos that form in simulations with a box size of $0.3 \ h^{-1}$ Mpc, and $\sim 10 - 100 \ M_\odot$ for the halos that form in simulations with a box size of $0.6 \ h^{-1}$ Mpc, though the mean maximum mass (based on the Kelvin-Helmholz time) in the smaller box is $\simeq 200 \ M_\odot$ and in the larger box is $\simeq 30 \ M_\odot$.

4.4.4 The formation of a Population III star in the presence of a soft UV background

Another important scenario for the formation of Population III stars involves the presence of a soft ultraviolet (SUV) background. As discussed in Section 4.2, massive primordial stars are copious emitters of ultraviolet radiation, particularly in the Lyman-Werner band $(11.18 - 13.6 \ eV)$ which is responsible for the photodissociation of molecular hydrogen. Since this radiation is below the ionization energy of atomic hydrogen it is predicted that photons in the Lyman-Werner band would form a nearly uniform background of soft ultraviolet light, which could significantly affect the formation of later generations of Population III stars due to the dissociation of molecular hydrogen. Previous work has been done on this subject by Machacek, Bryan & Abel [71] – however, the work presented here uses higher resolution calculations and examines more fully the evolution of a single halo.

The simulations are set up as described in Section 4.3 in an $0.3 \ h^{-1}$ Mpc box. A single cosmological realization is resimulated assuming a constant Lyman-Werner soft UV background with intensities of $F_{LW} = 0, 10^{-24}, 10^{-23}, 3 \times 10^{-23}, 10^{-22}, 10^{-21}$ and 10^{-20} ergs s^{-1} cm^{-2} Hz^{-1}, which covers a much wider range of parameter space than the results described by Machacek et al. The simulations are initialized at $z = 99$ and are evolved until the collapse of the core of the largest halo, which occurs at a range of redshifts. The simulations with the two highest SUV fluxes do not collapse before $z = 10$, when these two simulations are stopped.

Figure 4.24 shows mean halo quantities for several of these simulations at the redshift of collapse of the halo core. The top left panel shows the Lyman-Werner flux vs. halo collapse redshift for all of the simulations whose halos actually collapsed. The top right
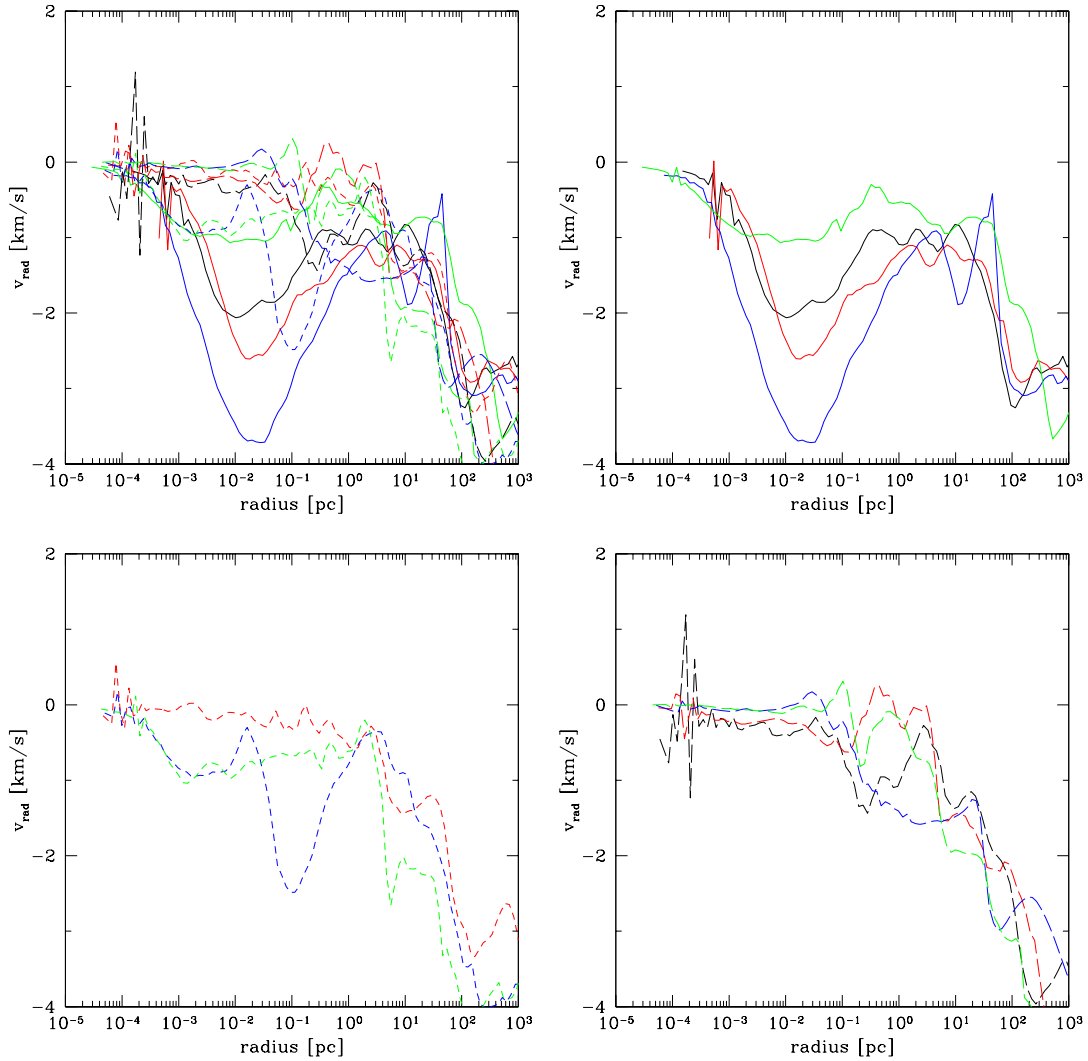
Figure 4.22: Mass-weighted, spherically-averaged baryon radial velocity as a function of radius for 11 different cosmological random realizations, chosen at an output time where peak baryon density values are approximately the same. There are three box sizes: $0.3 \ h^{-1}$ Mpc, $0.45 \ h^{-1}$ Mpc and $0.6 \ h^{-1}$ Mpc (comoving). One of the $0.45 \ h^{-1}$ Mpc simulations has been omitted since the simulation crashed before reaching a comparable density value. Top left panel: All 11 simulations plotted together. Top right panel: 0.3 h^{-1} Mpc box simulations. Bottom left panel: $0.45 \ h^{-1}$ Mpc box simulations. Bottom right panel: $0.6 \ h^{-1}$ Mpc box simulations.
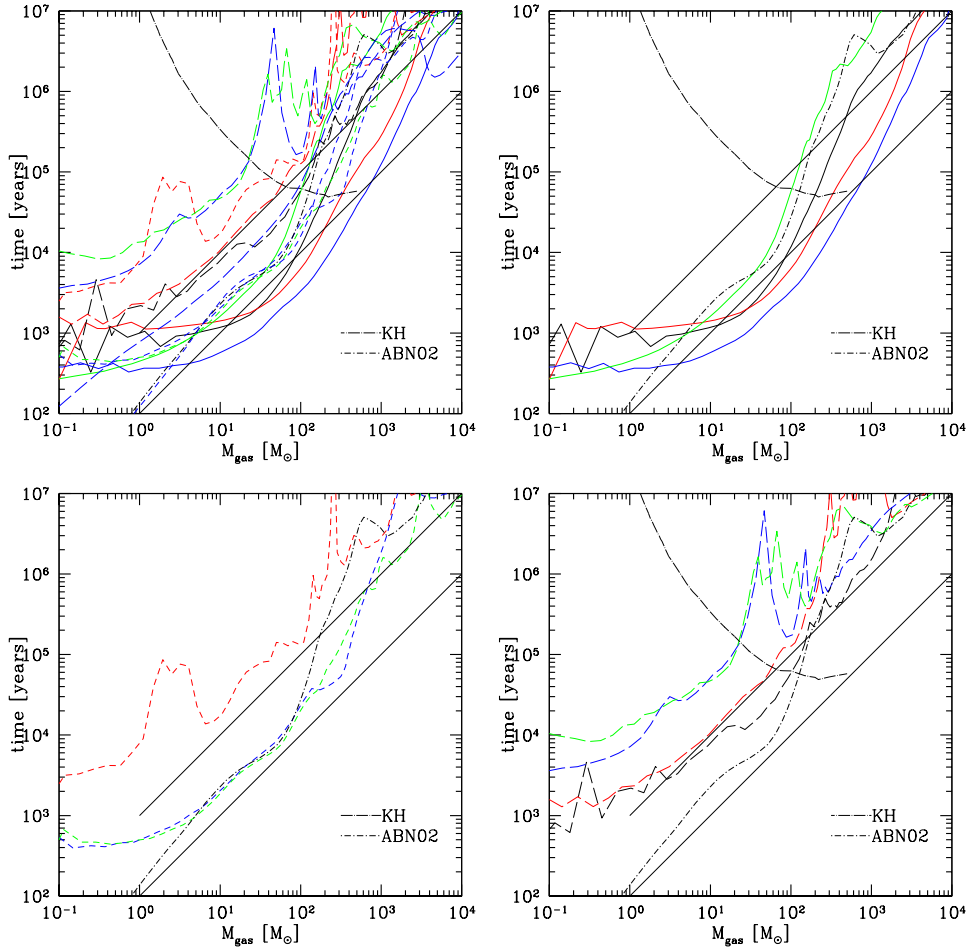
Figure 4.23: Mass-weighted, spherically averaged baryon accretion time as a function of radius for 11 different cosmological random realizations, chosen at an output time where peak baryon density values are approximately the same. There are three box sizes: 0.3 h^{-1} Mpc, 0.45 h^{-1} Mpc and 0.6 h^{-1} Mpc (comoving). One of the 0.45 h^{-1} Mpc simulations has been omitted since the simulation crashed before reaching a comparable density value. Top left panel: All 11 simulations plotted together. Top right panel: 0.3 h^{-1} Mpc box simulations. Bottom left panel: 0.45 h^{-1} Mpc box simulations. Bottom right panel: 0.6 h^{-1} Mpc box simulations. The baryon accretion time is defined as $T_{acc} \equiv M_{enc}/\dot{M}$, where M_{enc} is the enclosed baryon mass and $\dot{M} \equiv 4\pi r^2 \rho(r) v(r)$, with $\rho(r)$ and $v(r)$ being the baryon density and velocity as a function of radius, and $v(r)$ defined as being positive towards the center of the halo. The dot-long dashed line in each panel is the Kelvin-Helmholz time for a Population III star with a mass identical to the enclosed mass, as calculated from the results given by Schaerer. The dot-short dashed line in each panel is the baryon accretion time for the result in Abel, Bryan & Norman. The upper and lower diagonal solid black lines correspond to constant accretion rates of 10^{-3} and 10^{-3} M$_\odot$/yr, respectively.

143

panel shows the Lyman-Werner flux vs. virial mass of the eventual halo that formed for each simulation. Finally, the bottom panel shows the virial mass vs. collapse redshift for each of these calculations. The collapse redshift of the "control" simulation ($F_{LW} = 0$) is shown as a vertical blue dashed line in the top two panels and as a blue square in the bottom panel.

This figures shows that there is a clear relationship between the Lyman-Werner flux intensity and the collapse redshift and virial mass of the halo. A larger Lyman-Werner flux results in a later collapse time because the halo must be larger in order to have core densities high enough that significant amounts of molecular hydrogen can form in them. The final mass of the halo in the simulation with $F_{LW} = 10^{-22}$ is approximately five times that of the control simulation, and collapses significantly later in time. This agrees qualitatively with the results seen by Machacek, Bryan and Abel [71], who suggest that there is a "minimum halo mass" which is a function of the strength of the UV background. The practical effect of this is that as the Lyman-Werner UV background builds up the minimum halo mass which is necessary to form significant amounts of molecular hydrogen climbs, causing an overall suppression of the formation of Population III stars in halos with masses that are $\sim 10^6$ M$_\odot$. When the Lyman-Werner flux becomes extremely large, the formation of molecular hydrogen is almost entirely suppressed, resulting in termination of Pop III star formation in halos in this mass range. In this situation, primordial star formation cannot occur in halos this small – rather, the star formation must occur in halos that are massive enough that the mean gas temperature in the halo is at least 10^4 Kelvin, at which point the gas can cool efficiently via atomic line cooling. When a high enough density is reached through this cooling mechanism, the formation of molecular hydrogen can take place essentially independent of the strength of the UV background, allowing primordial star formation to occur. This mode of star formation has not been explored in depth by any published numerical calculations (though Bromm & Loeb [211] use a relatively poorly resolved calculation of the evolution of these halos to examine the possible formation of the first supermassive black holes), and the resulting IMF is unknown.

It is worth noting that we do not see the same functional form for the "threshold mass" of Machacek et al. They predict that the lowest halo mass that can collapse in a simulation with a uniform Lyman-Werner flux is

$$M_{TH}(M_\odot) = 1.25 \times 10^5 + 8.7 \times 10^5 \ \left(\frac{F_{LW}}{10^{-21}}\right)^{0.47} \tag{4.2}$$

Where F_{LW} is the Lyman-Werner flux in the same units as above. Our calculations agree with this result qualitatively: The Machacek fitting form is of the lowest possible halo mass that can collapse, whereas our halo is more representative of a "typical" halo, in the sense that its mass is approximately the average halo mass (as determined from previous sections). Of the halos that do collapse in our calculations, the halo mass at the

time of collapse is well-fit by the power law $M(F_{LW}) = 4.35 \times 10^5 \; (F_{LW}/10^{-24})^{0.27} \; M_\odot$ (excluding the $F_{LW} = 0$ case). Both of these functional forms are plotted in the top right panel of Figure 4.24, with the Machacek et al. result as a green dashed line and our fitting form as a red dashed line. The apparent lack of agreement is due to our simulation of a "typical" halo, whereas Machacek plots a threshold mass. Additionally, they use a cosmological model with somewhat different values for σ_8, Ω_m, Ω_Λ, Ω_b and h, which may contribute to the lack of agreement.

Figure 4.25 through 4.27 show spherically-averaged, mass weighted radial profiles of several baryon quantities of all simulations, including those whose largest halo did not collapse. Radial profiles for simulations which did undergo halo collapse are plotted when the central density reaches a set density ($n \simeq$ a few times 10^{10} cm^{-3}). Simulations which did not undergo halo collapse are shown at the last data output, $z = 10$.

Figure 4.25 shows the spherically-averaged radial profiles of baryon number density, baryon temperature, and enclosed mass as a function of radius. As in Section 4.4.3, the baryon density profiles and enclosed mass profiles are similar between the different calculations, which can be explained by the cooling properties of a primordial gas. The temperature profiles of the collapsed gas are similar at large radii, but in the center of the halo there is a trend towards simulations with higher Lyman-Werner fluxes having a higher core temperatures, with the results being separated essentially into two populations. The overall core temperature of the population with fluxes $F_{LW} \leq 10^{-24}$ ergs s^{-1} cm^{-2} Hz^{-1} is roughly 500 Kelvin, while the population with fluxes of $10^{-23} \leq F_{LW} \leq 10^{-22}$ has a central core temperature of approximately 1000 K. Simulations with $F_{LW} > 10^{-22}$ do not collapse by the end of the simulation and have significantly higher overall temperatures. The reason for this can be seen by examination of Figure 4.26, which plots the molecular hydrogen fraction, H^- fraction, and electron fraction of the baryon gas as a function of radius. The overall H_2 fraction in simulations with $F_{LW} \leq 10^{-24}$ ergs s^{-1} cm^{-2} Hz^{-1} is a factor of a few higher than the population with $10^{-23} \leq F_{LW} \leq 10^{-22}$, and simulations with a higher UV flux have very little H_2 overall. This trend is due to the photodissociation of molecular hydrogen by the soft UV background, which delays collapse of the halos by affecting cooling rates. Once the center of a halo reaches some critical density (which is a function of F_{LW}), H_2 formation can continue as before. However, at lower densities the H_2 fraction reaches some equilibrium with the UV background, where the rates of photodissociation and creation of H_2 are equal. This can be clearly seen outside of $r \sim 0.1$ parsec in the plot of H_2 fraction as a function of radius, where there is a monotonic decrease in the H_2 fraction outside the core with increasing UV flux.

As one might expect, the spread in halo core central temperatures produces somewhat different end results. Figure 4.27 shows the radial and circular baryon velocities as a function of radius, and the accretion time as a function of enclosed mass. Predictably, simulations with a lower core temperature tend to have a lower overall infall velocity of gas onto the central protostar, though there is some scatter in the result. This is most likely
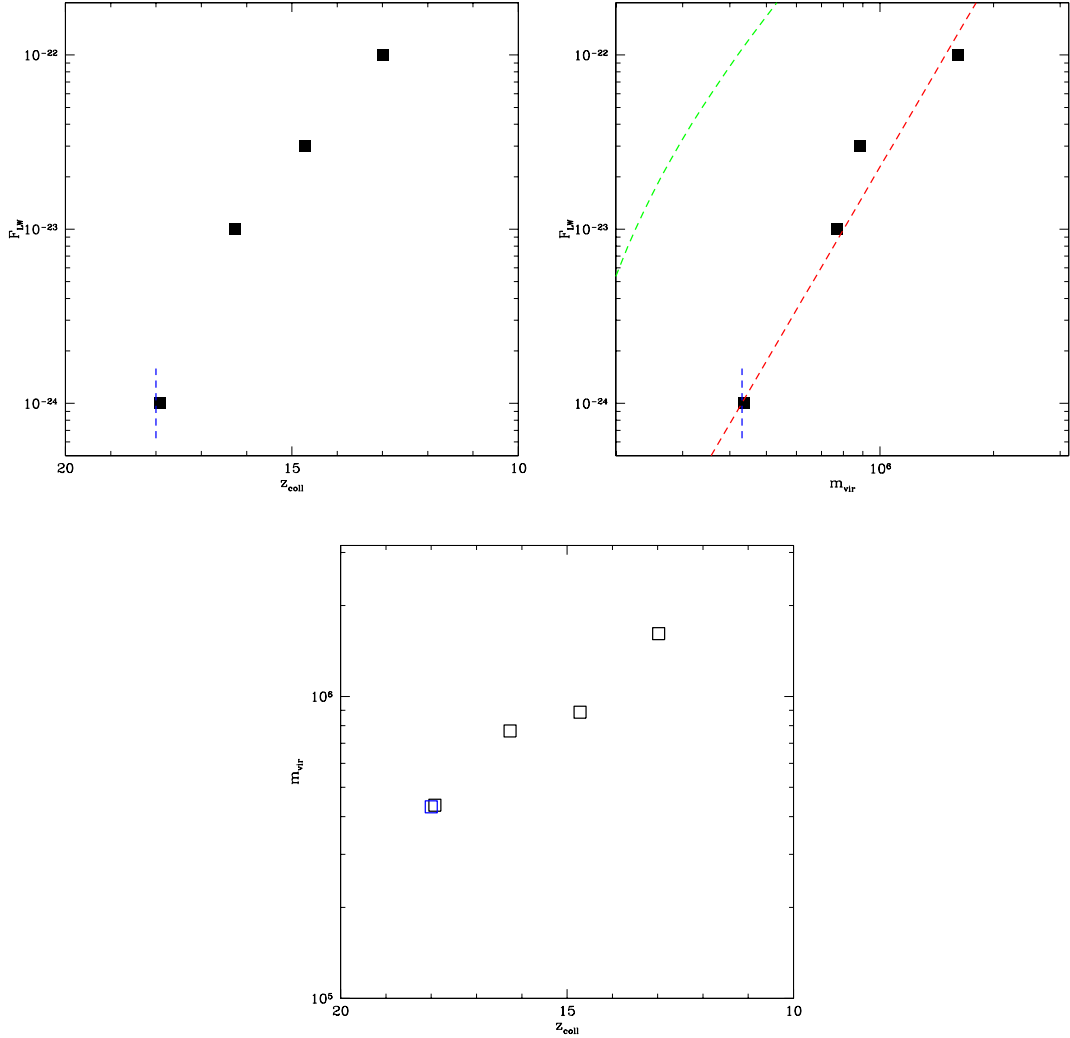
Figure 4.24: Mean halo quantities for several simulations with the same cosmic realization but a range of Lyman-Werner molecular hydrogen photodissociating flux backgrounds. Top left: Lyman-Werner flux vs. halo collapse redshift. Top right: Lyman-Werner flux vs. halo virial mass at collapse. Bottom: halo virial mass vs. collapse redshift. Simulations with values for the soft UV background of $F_{LW} = 10^{-21}$ and 10^{-20} did not collapse and are not shown. In the top two panels the collapse redshift/virial mass of the $F_{LW} = 0$ "control" result are shown as vertical blue dashed lines. In the top right panel the green dashed line corresponds to the fitting function for threshold mass from Machacek et al. (eqtn. 8), and the red dashed line corresponds to a simple power law, $M(F_{LW}) = 4.35 \times 10^5 \ (F_{LW}/10^{-24})^{0.27} \ \mathrm{M}_\odot$.

146

Figure 4.25: Mass-weighted, spherically-averaged baryon quantities as a function of radius for 7 simulations of the same cosmological realization and a range of soft UV backgrounds. Top left: number density as a function of radius. Top right: temperature as a function of radius. Bottom: enclosed mass as a function of radius. In all panels, the black long-dashed line corresponds to $F_{LW} = 0$, the black solid line to $F_{LW} = 10^{-24}$, the blue solid line to $F_{LW} = 10^{-23}$, the green solid line to $F_{LW} = 3 \times 10^{-23}$, the red solid line to $F_{LW} = 10^{-22}$, the black short-dashed line to $F_{LW} = 10^{-21}$, and the blue short-dashed line to $F_{LW} = 10^{-20}$. All simulations with $F_{LW} \leq 10^{-22}$ are shown at their redshift of collapse, while simulations with values for the soft UV background of $F_{LW} = 10^{-21}$ and 10^{-20} did not collapse and are shown at the last available redshift.
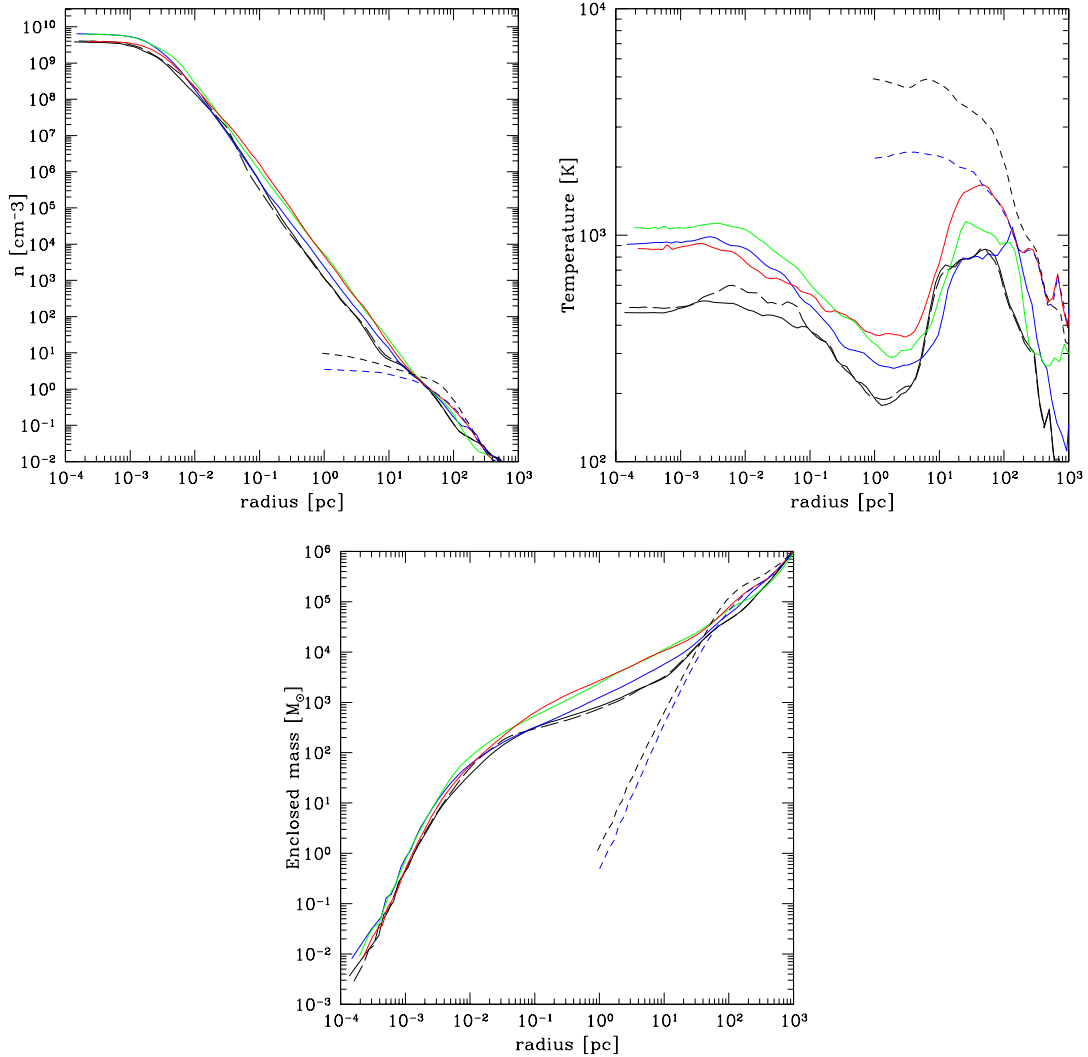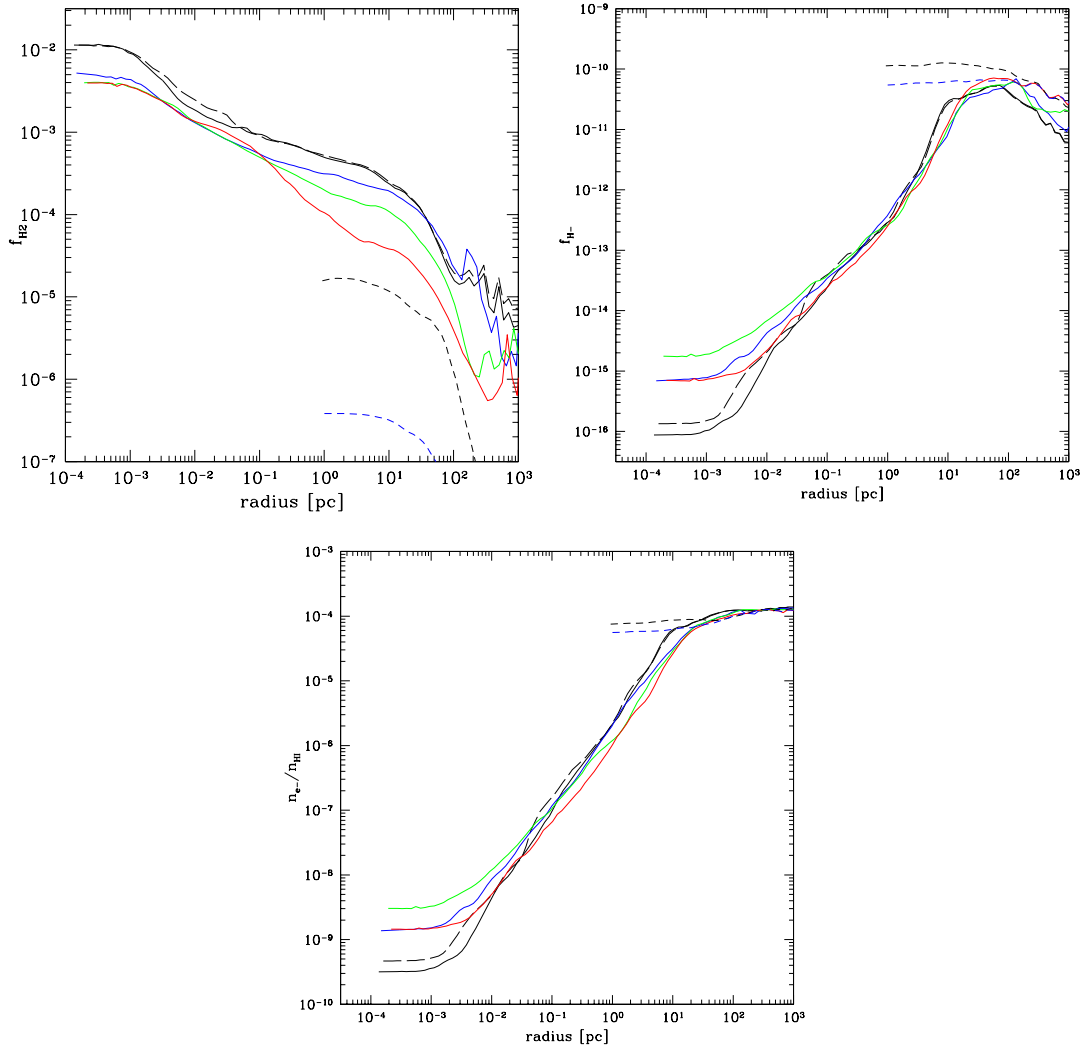
147

Figure 4.26: Mass-weighted, spherically-averaged baryon quantities as a function of radius for 7 simulations with the same cosmological realization and a range of soft UV backgrounds. Top left: molecular hydrogen fraction as a function of radius. Top right: H^- fraction as a function of radius. Bottom: electron fraction as a function of radius. In all panels, the black long-dashed line corresponds to $F_{LW} = 0$, the black solid line to $F_{LW} = 10^{-24}$, the blue solid line to $F_{LW} = 10^{-23}$, the green solid line to $F_{LW} = 3 \times 10^{-23}$, the red solid line to $F_{LW} = 10^{-22}$, the black short-dashed line to $F_{LW} = 10^{-21}$, and the blue short-dashed line to $F_{LW} = 10^{-20}$. All simulations with $F_{LW} \leq 10^{-22}$ are shown at their redshift of collapse, while simulations with values for the soft UV background of $F_{LW} = 10^{-21}$ and 10^{-20} did not collapse and are shown at the last available redshift.

due to the fact that the halos in these calculations do not exist in isolation – during the significant amount of time that the collapse of the halo core is delayed, structure formation is still taking place and the overall halo mass is being substantially increased by accretion, which may have some nonlinear effects on the halo temperature, molecular hydrogen fraction, and as a result the accretion rate onto the protostar. Regardless, the final estimate for the mass of the star, using the same criteria as in Section 4.4.1, suggests that the overall spread of final stellar masses is significantly enlarged by the addition of a soft UV background. Halos with larger SUV fluxes tend to have higher temperatures, and thus higher accretion rates and possibly higher stellar masses.

Figures 4.28 through 4.30 show two-dimensional, mass weighted distribution functions of several quantities which illustrate the overall effects of the photodissociating flux. All panels are shown at their redshift of collapse or (for those that do not collapse) the final output of the simulation at $z = 10$. Each panel has 10 contours spaced equally in logarithmic intervals between the lowest and highest values in the panel.

Figure 4.28 shows the two-dimensional distribution function of baryon temperature vs. baryon overdensity (δ) for all of the simulations simulations discussed in this section, and Figure 4.29 shows the two-dimensional distribution of molecular hydrogen fraction as a function of overdensity. These two plots illustrate the important density thresholds related to the chemistry and cooling properties of molecular hydrogen. The "knee" seen in the temperature-overdensity plot at $\delta \sim 100$ corresponds to a critical density at which the molecular hydrogen formation time scale becomes less than the Hubble time. This is due to the molecular hydrogen formation rate increasing with density. There is a corresponding "knee" in the H_2 - baryon overdensity distribution function at this overdensity. At overdensities between 10^2 and 10^5 the temperature decreases with increasing density, and the molecular hydrogen fraction continues to grow. At an overdensity of approximately 10^5 the ro-vibrational levels of H_2 are populated at their equilibrium value and the cooling rate becomes independent of density, which corresponds to an increase in gas temperature with increasing density. Finally, at number densities of $n \sim 10^9 - 10^{10}$ cm^{-3} (overdensities of $\sim 10^{11}$) the three-body molecular hydrogen formation becomes dominant and H_2 is formed very rapidly with increasing density. This can be seen as another "knee" in the $H_2 - \delta$ distribution function at overdensities of $\sim 10^{11}$, though the cooling properties of the gas still remains density independent. Simulations with a Lyman-Werner background flux that is high enough to completely suppress the formation of molecular hydrogen ($F_{LW} \geq 10^{21}$) cannot cool efficiently and therefore cannot collapse to overdensities higher than $\sim 10^3$.

From the standpoint of Population III star formation,the practical effects of the cooling properties of H_2 can be summed up in Figure 4.30, which is the two-dimensional mass-weighted distribution function of the Jeans mass (which scales as $\sim T^{3/2}/\rho^{1/2}$) versus overdensity. The Jeans mass (or, more precisely, the Bonnor-Ebert critical mass, which differs from the Jeans mass by a numerical constant) controls the mass scale at
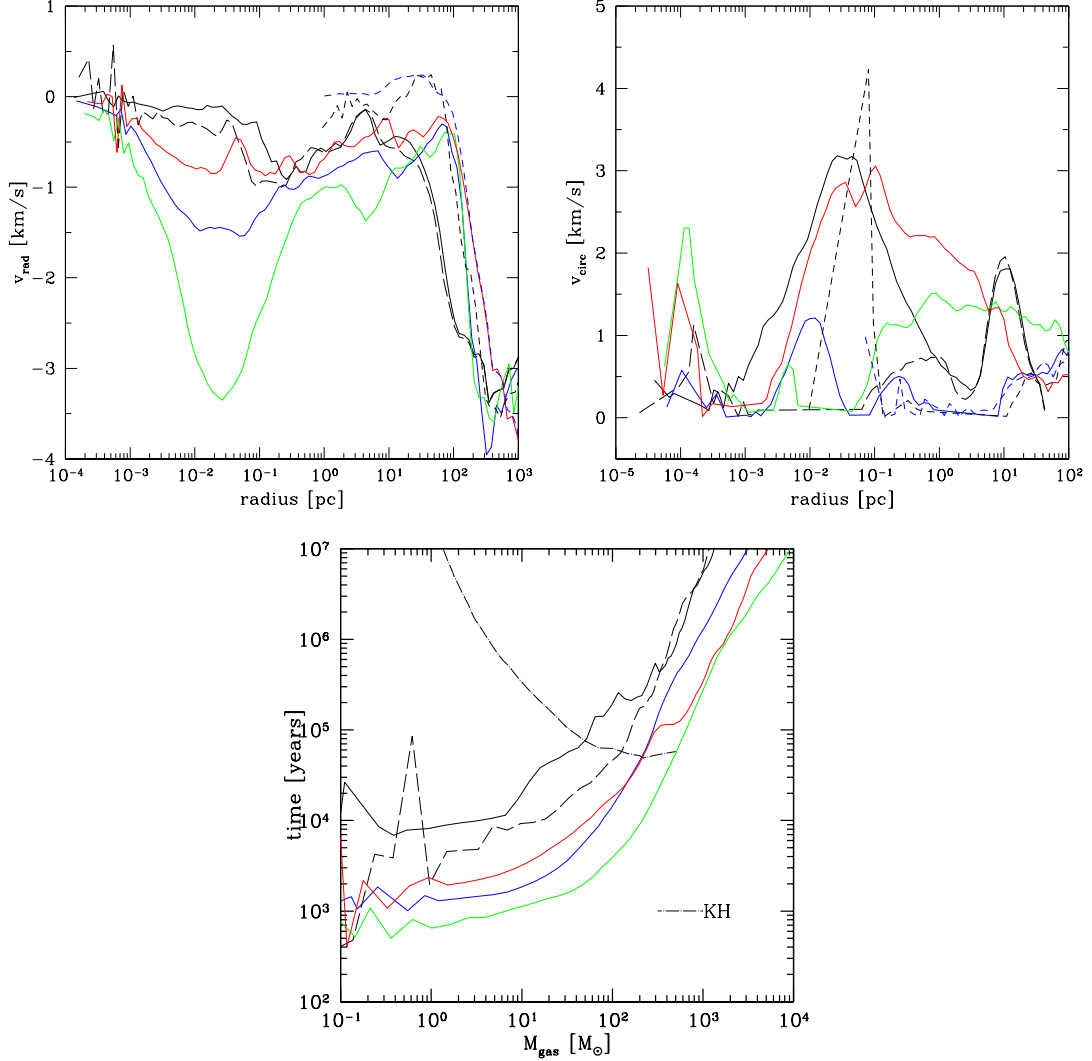
Figure 4.27: Mass-weighted baryon quantities for 7 simulations with the same cosmo-
logical realization and a range of soft UV backgrounds. Top left: spherically-averaged
radial velocity as a function of radius. Top right: cylindrically-averaged circular velocity
as a function of radius. Bottom: Accretion time (defined as in Figure 4.23) as a function
of enclosed mass. In all panels, the black long-dashed line corresponds to $F_{LW} = 0$, the
black solid line to $F_{LW} = 10^{-24}$, the blue solid line to $F_{LW} = 10^{-23}$, the green solid
line to $F_{LW} = 3 \times 10^{-23}$, the red solid line to $F_{LW} = 10^{-22}$, the black short-dashed line
to $F_{LW} = 10^{-21}$, and the blue short-dashed line to $F_{LW} = 10^{-20}$. All simulations with
$F_{LW} \leq 10^{-22}$ are shown at their redshift of collapse, while simulations with values for
the soft UV background of $F_{LW} = 10^{-21}$ and 10^{-20} did not collapse and are shown at the
last available redshift.

which fragmentation of the gas via gravitational instability can occur. At low densities, the overall temperature is high and therefore the Jeans mass is quite high – at least 10^5 $M_\odot$ for $\delta \sim 10^2 - 10^3$. However, at higher densities the temperature drops rapidly up to $\delta \sim 10^5$, resulting in a corresponding rapid drop in the Jeans mass. At these density scales the Jeans mass is still too high for efficient fragmentation. Once the cooling rate becomes independent of density the temperature begins to climb as a function of overdensity, but at a fairly low rate, so the Jeans mass continues to drop, though not as rapidly. Finally, at an overdensity of $\sim 10^{11}$ (after the 3-body process begins to dominate) the Jeans mass drops below 100 $M_\odot$, which is roughly equivalent to the total amount of gas that has reached that overdensity. In principle one might suppose that the gas in the halo core could begin to fragment at this point, but no evidence of fragmentation has been found in any of the simulations that we have examined.

4.5   Discussion

In this chapter we have explored several aspects of the formation of Population III stars in a ΛCDM universe. This section summarizes some of the processes neglected in our calculations and also attempts to put some of the results in context.

The results presented in Section 4.4.3 demonstrate that there is a great deal of scatter between the bulk halo properties such as overall virial mass, collapse redshift, and mean halo temperature among the twelve simulations shown. However, the final state of the density profile is extremely similar between all of the calculations. This is entirely due to the chemical and cooling properties of the primordial gas – the minimum temperature of the gas (which is determined by its chemical composition) creates a density profile that goes as r^{-2} for any gas cloud which is only supported by thermal pressure. This seems to be true for the gas contained in the halos out of which Population III stars form, so it is reasonable to expect consistent density profiles on halo scales.

Though there is consistency in the bulk halo properties, a detailed examination of the gas properties which may contribute significantly to the final Pop III star mass, such as the core baryon temperature and accretion rate onto the forming primordial protostar, show a tremendous amount of scatter. This scatter appears to be due to variations in the molecular hydrogen content of the halo on large scales, which is brought on by differences in halo temperature as a result of varied merger rates between simulations. There appears to be a systematic effect between the simulation box size and the mean temperature, with larger boxes (which have more large-scale power and overall a more rapid merger history) having higher overall halo temperatures and lower accretion rates. The higher temperatures result in somewhat larger molecular hydrogen mass fractions, which cause the halo core to cool more rapidly during its eventual collapse. Since the accretion onto the primordial protostar is primarily subsonic, the accretion rate depends on the sound
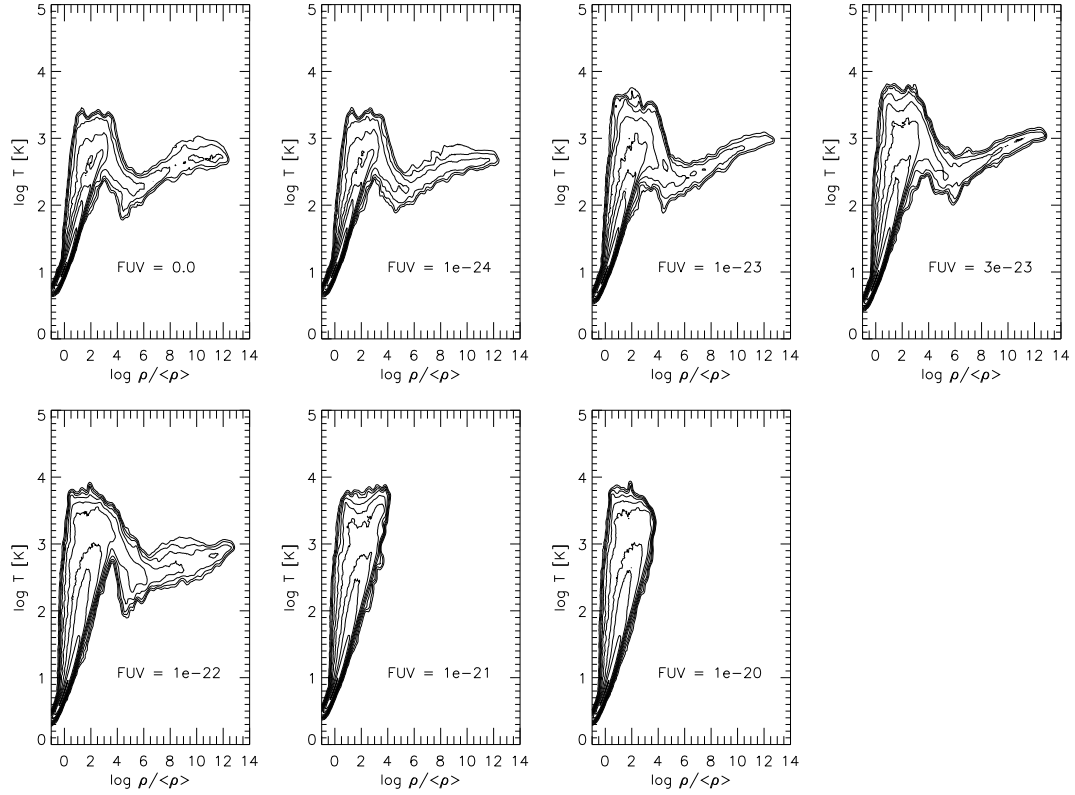
Figure 4.28: Mass-weighted two-dimensional distribution functions of baryon temperature vs. baryon overdensity for seven simulations with the same cosmological realization and a range of soft UV backgrounds. The strength of the UV background is marked in each panel. All simulations with $F_{LW} \leq 10^{-22}$ are shown at their redshift of collapse, while simulations with values for the soft UV background of $F_{LW} = 10^{-21}$ and 10^{-20} did not collapse and are shown at the last available redshift. Each panel has 10 contours equally spaced in logarithmic intervals between the maximum and minimum values in that panel.

Figure 4.29: Mass-weighted two-dimensional distribution functions of molecular hydrogen fraction vs. baryon overdensity for seven simulations with the same cosmological realization and a range of soft UV backgrounds. The strength of the UV background is marked in each panel. All simulations with $F_{LW} \leq 10^{-22}$ are shown at their redshift of collapse, while simulations with values for the soft UV background of $F_{LW} = 10^{-21}$ and 10^{-20} did not collapse and are shown at the last available redshift. Each panel has 10 contours equally spaced in logarithmic intervals between the maximum and minimum values in that panel.
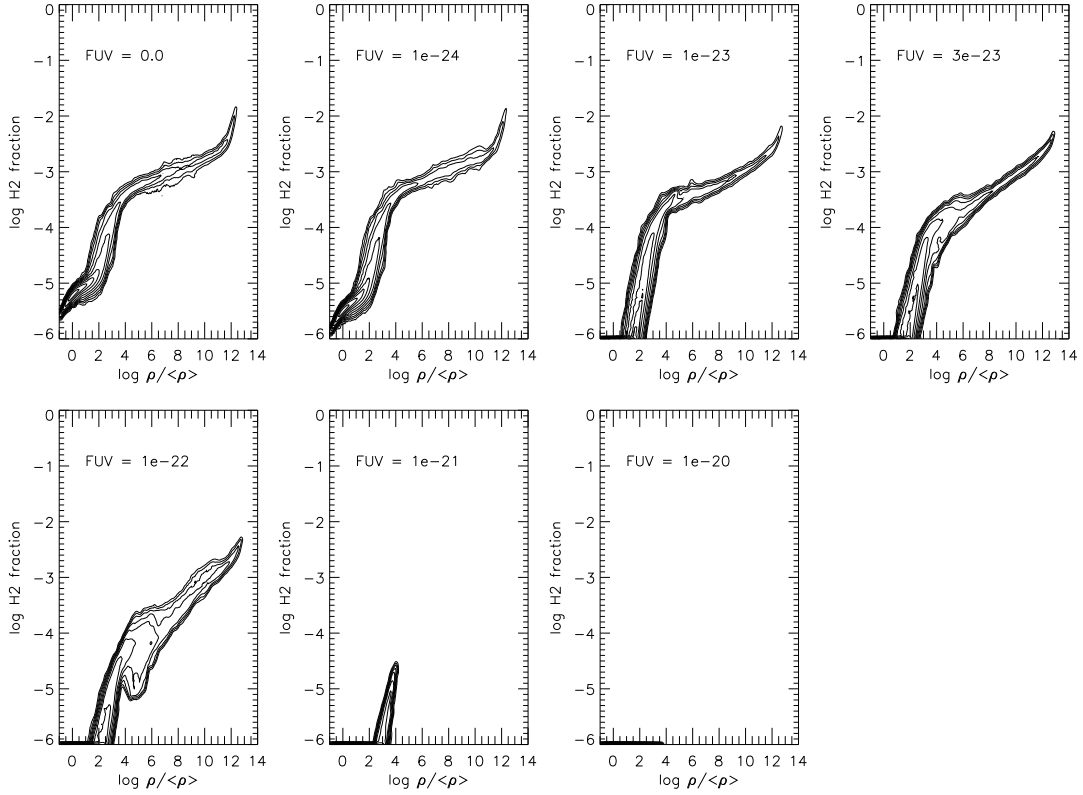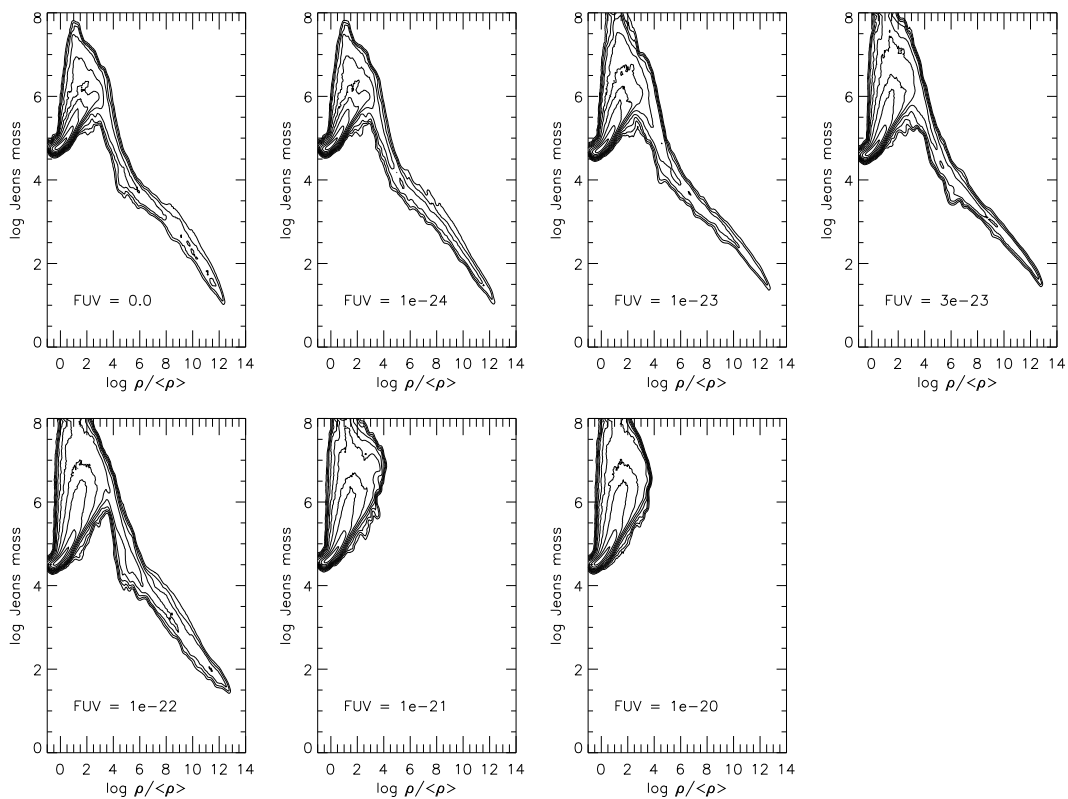
Figure 4.30: Mass-weighted two-dimensional distribution functions of cell Jeans mass vs. baryon overdensity for seven simulations with the same cosmological realization and a range of soft UV backgrounds. The strength of the UV background is marked in each panel. All simulations with $F_{LW} \leq 10^{-22}$ are shown at their redshift of collapse, while simulations with values for the soft UV background of $F_{LW} = 10^{-21}$ and 10^{-20} did not collapse and are shown at the last available redshift. Each panel has 10 contours equally spaced in logarithmic intervals between the maximum and minimum values in that panel.

154

speed cubed, with lower core temperatures directly resulting in lower accretion rates.

After the onset of collapse, the evolution of the core of the halo (roughly the inner few thousand solar masses) becomes effectively decoupled from the halo envelope since the time scales become much shorter within the halo core. This tells us that while the formation of the initial primordial protostellar cloud is strongly coupled to the time scales associated with cosmological structure formation, once the cloud has collapsed we can treat the core of the halo separately from the rest of the calculation. This decoupling will become highly useful when more detailed calculations of the evolution of Population III protostars, including more complicated physics such as radiative transfer and protostellar accretion models, are performed, and will save us significant computational cost.

The observation that the rate of accretion onto the primordial protostar varies systematically as a function of box size, with larger box sizes having an overall lower accretion rate, has significant implications for both reionization and metal enrichment of the early universe. The accretion rate results cannot be proven to be converged yet, due to noise and small number statistics, though the 0.45 and 0.6 h^{-1} Mpc boxes seem to have overall similar accretion rates. We make an estimate of the minimum possible accretion rate by observing that molecular hydrogen is only effective at cooling the primordial gas down to approximately 200 Kelvin, which gives us an accretion rate of $\dot{M}_* \simeq 5 \times 10^{-4}$ M$_\odot$/year, which is reasonably close to the lower envelope of accretion rates observed in the 0.6 h^{-1} Mpc box calculations. Though this implies convergence, it would be prudent to perform another suite of calculations at an even larger box size to be sure.

If in fact a lower overall accretion rate results in a less massive population of stars, these objects will be much less effective at ionizing the intergalactic medium (since they produce overall fewer UV photons per baryon) and will produce a completely different nucleosynthetic signature. This is important because the measurement of the polarization of the cosmic microwave background by the WMAP satellite implies early reionization, which possibly implies a significant contribution from extremely massive Population III stars, whereas observations of ultra metal poor stars in the galactic halo see abundance ratios that do not agree with numerical predictions for the abundance ratios of extremely massive primordial stars. At this point it is difficult to say what accretion rate is most common during Population III star formation. In particular, once a soft ultraviolet background begins to build up and cause the photodissociation of molecular hydrogen the overall halo core temperatures may rise, causing an increase in the baryon accretion rate. Wise & Abel [97] use Press-Schechter models of Population III star formation to predict a slowly rising Lyman-Werner background which provides some support to this idea. This suggests that further calculations including larger simulation volumes as well as a soft UV background will be necessary to make a definitive statement about the most common accretion rates. Additionally, these calculations completely neglect the mode of primordial star formation that takes place in halos whose virial temperatures are above

155

10^4 K. Cooling in these systems is dominated by atomic hydrogen line emission and, particularly in the presence of a strong soft UV background, may result in a much larger amount of cold gas distributed in a different manner than in the systems simulated in this thesis, which have mean virial masses of a few times 10^5 $M_\odot$ and virial temperatures of around 1000 K.

In Section 4.4.2 we examined angular momentum transport in the collapsing halo core. This appears to be a robust result, and the primary mode of angular momentum redistribution appears to be due to turbulence. Unfortunately it is somewhat difficult to analyze this effect using the standard analytical formalism for angular momentum transport in accretion disks since the collapsing halo core is approximately spherical. It seems that a more complicated method of analyzing the turbulence properties within the halo core, such as structure functions, may be in order. Additionally, the efficiency of turbulent angular momentum transport in a quasistatically collapsing spheroid has not been studied analytically or numerically, and a better physical understanding of the situation may result from developing new analytics and idealized numerical test problems.

It is not completely clear what drives the turbulence in the halo core. There is accretion of gas into the core of the halo, and this provides a possible mechanism for driving turbulence. Also, during the quasistatic collapse of the halo core the gas is subject to significant cooling, which may drive turbulence via thermal instabilities. This seems less likely, because the sound speed is comparable to the speed of collapse, which serves to smooth the overall density perturbation. More investigation is necessary, perhaps using idealized numerical simulations, to understand the precise mechanism for driving the turbulence seen in the collapsing halo core.

Unlike galactic star formation at the present epoch, the collapsing cosmological halo core has little angular momentum from the outset – the "angular momentum problem" that plagues present-day star formation simply doesn't appear to be an issue in the Population III star formation scenario. During the quasi-static collapse of the halo core the gas is never rotationally supported – the gas is essentially completely held up by thermal pressure. It appears that the small amount of angular momentum that is actually transported is not a critical factor in the cloud core's collapse.

As discussed in Section 4.4.2, the angular momentum transport result does not appear to be due to numerical effects. Unfortunately, it is particularly difficult to quantify numerical viscosity due to finite resolution in an adaptive mesh refinement code, since the overall grid resolution can vary tremendously. Essentially the only reliable way to quantify numerical viscosity in an AMR code is to pose a problem with an analytical solution that explicitly includes a physical viscosity and then simulate it with adaptive mesh code using the Eulerian equations for fluid flow. Since these equations assume zero physical viscosity, any viscous effects observed are completely numerical, and the analytical problem can be used to extract a value for the numerical viscosity. This is a challenging task, and the measured numerical viscosity is most likely dependent on the

details of the test problem and can vary strongly depending on the physical system being modeled.

The primordial chemistry model used in these calculations ignores the effects of deuterium, lithium, and the various molecules they form between these elements and ordinary hydrogen. Deuterium and lithium have been shown to be unimportant in the temperature and density regimes that we have examined in this chapter. However, it is possible that they may be relevant in other situations of importance to Population III star formation – in particular, regions which have been ionized to very high electron fractions may experience significant cooling from the HD molecule, which due to its permanent dipole moment makes it more than 100 times more effective as a cooling agent than molecular hydrogen (per molecule), and has the potential to cool gas down to approximately the temperature of the cosmic microwave background, which scales with redshift as $T_{cmb}(z) = 2.73 \times (1+z)$ K. This gives a minimum baryon temperature of approximately 55 Kelvin at $z = 20$ and could further reduce the minimum accretion rate onto a primordial protostar by a factor of two, to $\dot{M}_{min} \simeq 2.5 \times 10^{-4}$ M$_\odot$/year.

The effects of magnetic fields are completely ignored in the simulations discussed in this thesis. We can justify this by examining the magnetic field necessary to delay the collapse of the halo core. If one assumes that the halo core can be represented reasonably well by an isothermal sphere of constant density (which is reasonable at the onset of halo collapse), we can use the virial theorem to estimate the strength of the magnetic field which is necessary to support the collapse of the halo against gravity. Assuming flux freezing and a uniform magnetic field, a magnetically critical isothermal sphere has a mass-to-flux ratio of

$$\frac{M_{cl}}{\Phi_B} = \frac{1}{\sqrt{31G}} \qquad (4.3)$$

Where M$_{cl}$ is the mass of the halo, $\Phi_b = \pi R_{cl}^2 B_{cl}$ is the magnetic flux in the cloud (with R$_{cl}$ and B$_{cl}$ being the cloud radius and magnetic field strength, respectively), and G is the gravitational constant. Reasonable values for M$_{cl}$ and R$_{cl}$ are $\simeq 2 \times 10^3$ M$_\odot$ and 4 parsecs, respectively, which gives us a value of the magnetic field of B$_{cl} = 1.21 \times 10^{-5}$ G. The mean density of the cloud is n$_{cl} \simeq 300$ cm^{-3} and the mean density of the universe at $z = 18$ (the redshift that our cloud collapses) is $\simeq 0.003$ cm^{-3}, so if we assume a spherical collapse from the mean cosmic density assuming flux freezing, we see that the ratio of the magnetic field in the cloud to the mean universal magnetic field is

$$\frac{B_{cl}}{B_{igm}} = \left(\frac{n_{cl}}{n_{igm}}\right)^{2/3} \qquad (4.4)$$

This gives us a mean magnetic field of $B_{IGM} \simeq 3.5 \times 10^{-9}$ G at $z \simeq 18$. Since there are no known objects that may produce magnetic fields between recombination

$(z \sim 1100)$ and the epoch of Pop III star formation, and the magnetic field scales with the expansion of the universe as $(1 + z)^2$, we estimate that in order for magnetic fields to be dynamically important in the formation of Population III stars the magnetic field strength at recombination must be $B_{rec} \sim 10^{-5}$ G. The current observational upper limit to magnetic field strength at recombination (albeit at large scales) is B $\leq$ 3 x 10^{-8} G as measured at the present epoch [29], which corresponds to a magnetic field at recombination of approximately 4×10^{-2} G. This is three orders of magnitude higher than needed to be dynamically relevant for Population III star formation! However, there are no known mechanisms that can produce a magnetic field of that magnitude that have not been ruled out due to other observational limitations. Currently, the most plausible mechanisms for creating magnetic fields at recombination suggest that field strengths are on the order of 10^{-23} G at recombination [33]. Given the observational uncertainty, it seems reasonable to ignore this effect, though future simulations will certainly include magnetic fields with a variety of field strengths and physical scales..

Assuming that the magnetic field at that epoch was strong enough to be dynamically important, we can calculate the effect that this has on the collapse of the star. Due to the low electron fraction in the halo core (which has electron densities comparable to or lower than that observed in present-day molecular cloud cores), the assumption of flux freezing in the magnetic field is not valid. Magnetic fields couple to charged particles (electrons and ions), and these charged particles interact with the neutral medium. At high levels of ionization collisions between charged and neutral particles are frequent, implying that the magnetic field is strongly coupled to the gas. However, at low levels of ionization there are few charged particles, and the coupling with the neutral gas is weak. In an object that is subject to a gravitational acceleration this produces a relative drift of charged and neutral particles which allows the neutral gas to decouple from the magnetic field. This effect is known as "ambipolar diffusion," and is believed to be an extremely important process in galactic star formation. The retardation effect that ambipolar diffusion may have on the collapse of the halo core can be estimated by examining the relative timescales of ambipolar diffusion and halo collapse. The ambipolar diffusion timescale can be estimated as

$$\tau_{AD} = \frac{L}{v_D} \simeq 2 \times 10^6 \; \frac{x_i}{10^{-7}} \; years \tag{4.5}$$

Where L and v_D are a characteristic length scale and the neutral-ion relative drift velocity, respectively, and x_i is the overall ionization fraction. A proxy for the halo collapse time scale is the free fall time, which for a spherical system is

$$\tau_{ff} = \left(\frac{3\pi}{32G\rho}\right)^{1/2} \simeq \frac{5 \times 10^7}{n^{1/2}} years \tag{4.6}$$

where n is the particle number density in particles per cubic centimeter and G is the gravitational constant. The relevance of ambipolar diffusion can be estimated by taking the ratio of these two quantities, which is known as the "collapse retardation time," ν_{ff}. Substituting in equations 4.5 and 4.6, we see that

$$\nu_{ff} \equiv \frac{\tau_{AD}}{\tau_{ff}} \simeq 4 \times 10^5 x_i n^{1/2} \tag{4.7}$$

Examination of figures 4.4 and 4.5 show that at the final timestep in the calculation, the number density can be fitted by a power law and is roughly $n(r) \simeq 10^3 \ (r/pc)^{-2} \ \text{cm}^{-3}$ while the ionization fraction scales roughly as $x_i(r) \simeq 10^{-6} \ (r/pc)$. Plugging these into equation 4.7 shows that $\nu_{ff} \simeq 13$ is constant with radius. This is only a crude approximation, since the free fall time really should depend on the mean number density instead of the number density at a given radius. However, considering the rapid falloff of density, n(r) is a reasonable approximation of n – strictly speaking, for a cloud with a density profile that scales as r^{-2} over many orders of magnitude in radius, the mean density is equal to 3 $n(r)$, so our estimate of the free fall time is too high by a factor of $\sqrt{3}$. Plugging this in to the equation, we get that $\nu_{ff} \simeq 23$ everywhere, which indicates significant delay in collapse with respect to the free fall time. However, the relevant time scale in this case is more appropriately the quasistatic collapse time, which is approximated as $\tau_{qs} \simeq L/v_r$. Figure 4.6 shows that the mean radial velocity at the scales of interest ($\sim 2-3$ parsecs) is roughly 0.5 km/s. This corresponds to $\tau_{qs} \sim 4 \times 10^6$ and scales linearly with the radius. Comparison with the ambipolar diffusion time scale shows that τ_{AD} and τ_{qs} are within a factor of two of each other, which suggests that the presence of a magnetic field would not significantly impede the collapse of the halo core for the quasistatic collapse case.

Section 4.4.4 discusses the formation of Population III stars in simulations with a constant soft UV background. Our results agree well qualitatively with that of Machacek, Bryan & Abel [71] – we both find that a soft UV background can delay the cooling and collapse of small ($\sim 10^6 \ \text{M}_\odot$) halos, and that increasing the soft UV background increases the minimum halo mass required for a halo to collapse. Machacek et al. derived a mass threshold for collapse as a function of the Lyman-Werner background flux that agrees well with our simulations, though the halo masses in our calculation are significantly higher. This is due to the halo that we examine being an average halo rather than at the plausible halo minimum mass. If we perform these calculations for large number of stars in a range of cosmological realizations it seems reasonable that the results from our lower-mass halos would agree more completely with their work. Future large volume, high-resolution calculations will further test the results of Machacek et al. at large boxes and for more halos. Our work is an improvement upon that of Machacek et al. because our simulations are much more highly resolved and we examine the evolution of a single halo over a much wider range of soft UV background fluxes.

In the calculations that we performed using a constant soft UV background we completely ignore self-shielding by molecular hydrogen. Though this effect could in principle

be important, the actual column densities of molecular hydrogen are typically far too small to actually block the soft UV flux. According to Machacek et al. (and references therein), a column density of 5×10^{14} cm^{-2} is enough for shielding to become important. However, this was derived for a static distribution of H$_2$, while the Lyman-Werner band consists of hundreds of individual lines whose width in this case is dominated by Doppler broadening. It is useful to note in this case that the average line width is ~ 2 km/s and the RMS baryon velocity in our calculations are ~ 4 km/s. In order for self-shielding to be important in the case of a turbulent medium the column density must be much higher. Typical maximum H$_2$ column densities in our calculations are on the order of 10^{16-17} cm^{-2}, but these occur late in the collapse of the core, and in the highest density regions the cooling and H$_2$ production times are much shorter than the photodissociation time scale, at which point self-shielding becomes unimportant.

As discussed previously, the simulation volumes used by our soft UV background calculations are rather small. The results of this is that the largest halo in our calculation has a virial temperature which is significantly below 10^4 K, which is when cooling via atomic hydrogen lines becomes an effective means of cooling halos. It is possible to produce halos that are this large without them having undergone previous epochs of star formation by having a very strong soft UV background. When the center of this type of halo cools via atomic lines to a large enough density, rapid molecular hydrogen formation will take place essentially independent of the strength of the soft UV background and the gas will be able to cool down to $\simeq 200$ K very quickly. Since these halos are more than an order of magnitude larger than those that we have considered in this project, presumably the reservoir of cold, dense gas in the center of the halo will also be correspondingly large. In this case, the amount of cold, dense gas will almost certainly exceed the Jeans mass by large factors, which in principle would make it possible for multiple Population III stars to form in a single halo, as opposed to the single star that we see forming at the center of halos in the simulations analyzed in this work. Further work will be necessary to understand how these larger halos form stars, and the potential IMF of the stars forming in them.